European Journal of Medicinal Chemistry 252 (2023) 115297

Contents lists available at ScienceDirect

European Journal of Medicinal Chemistry

journal homepage: www.elsevier.com/locate/ejmech

Research paper

Targeting the multifaceted neurotoxicity of Alzheimer's disease by tailored functionalisation of the curcumin scaffold

Ersilia De Lorenzi [a], Francesca Seghetti [b,2], Andrea Tarozzi [c], Letizia Pruccoli [c], Cecilia Contardi [a], Massimo Serra [a], Alessandra Bisi [b], Silvia Gobbi [b], Giulio Vistoli [d], Silvia Gervasoni [d,3], Carla Argentini [e], Giulia Ghirardo [e], Giulia Guarato [e], Genny Orso [e], Federica Belluti [b,*], Rita Maria Concetta Di Martino [b,1,4], Morena Zusso [e,4]

[a] Department of Drug Sciences, University of Pavia, Viale Taramelli 12, 27100 Pavia, Italy
[b] Department of Pharmacy and Biotechnology, Alma Mater Studiorum-University of Bologna, Via Belmeloro, 6, 40126 Bologna, Italy
[c] Department for Life Quality Studies, Alma Mater Studiorum-University of Bologna, Corso d'Augusto 237, 47921 Rimini, Italy
[d] Department of Pharmaceutical Sciences, University of Milan, Via Mangiagalli 25, 20133 Milan, Italy
[e] Department of Pharmaceutical and Pharmacological Sciences, University of Padua, Largo Meneghetti 2, 35131 Padua, Italy

ARTICLE INFO

Keywords:
Alzheimer's disease
Amyloid beta oligomers
Curcumin analogues
Natural products
Drosophila Melanogaster model
Neuroinflammation
Oxidative stress

ABSTRACT

Simultaneous modulation of multifaceted toxicity arising from neuroinflammation, oxidative stress, and mitochondrial dysfunction represents a valuable therapeutic strategy to tackle Alzheimer's disease. Among the significant hallmarks of the disorder, Aβ protein and its aggregation products are well-recognised triggers of the neurotoxic cascade. In this study, by tailored modification of the curcumin-based lead compound **1**, we aimed at developing a small library of hybrid compounds targeting Aβ protein oligomerisation and the consequent neurotoxic events. Interestingly, from *in vitro* studies, analogues **3** and **4**, bearing a substituted triazole moiety, emerged as multifunctional agents able to counteract Aβ aggregation, neuroinflammation and oxidative stress. *In vivo* proof-of-concept evaluations, performed in a *Drosophila* oxidative stress model, allowed us to identify compound **4** as a promising lead candidate.

1. Introduction

Alzheimer's disease (AD) affects 47 million people worldwide and is the most prevalent neurological disorder. In the absence of effective therapeutic strategies and a scenario of an ageing population, the increase rates are probably projected to reach beyond 152 million by 2050 [1].

The recognised neuropathological hallmarks of AD patients are senile plaques (SPs), which derive from the aggregation of amyloid β (Aβ) peptides, and neurofibrillary tangles, which are composed of aggregated hyperphosphorylated tau protein. Aβ protein accumulation and aggregation in brain tissue are supposed to represent one of the primary critical events triggering AD pathogenesis. The amyloid cascade hypothesis, officially postulated by Hardy and Higgins in 1992, has described the neuropathological consequences of Aβ aggregation and deposition (loss of cognitive functions, neuronal cell death and vascular damage) and over the last three decades has represented an essential focus of AD research programs and clinical trials [2,3].

Abbreviations: AD, Alzheimer's disease; Aβ, Amyloid β; AβOs, Amyloid β oligomers; CAT, catalase; CNS, central nervous system; CuAAC, copper-catalysed alkyne-azide cycloaddition; curc, curcumin; DMEM, Dulbecco's modified eagle's medium; ELISA, enzyme-linked immunosorbent assay; GPx, glutathione peroxidase; GSH, glutathione; HFIP, 1,1,1,3,3,3-hexafluoropropan-2-ol; HMW Aβ42Os, high molecular weight Aβ42 oligomers; IL-1β, interleukin-1β; IL-6, interleukin-6; LMW Aβ42Os, non-toxic low molecular weight Aβ42 oligomers; LPS, lipopolysaccharide; NPs, natural products; Nrf2, nuclear factor erythroid 2-related factor 2; PAINS, pan-assay interference; ROS, reactive oxygen species; SOD, superoxide dismutase; SPs, senile plaques; *t*-BuOOH, *tert*-butyl hydroperoxide; TNF-α, tumour necrosis factor-α.

* Corresponding author.
E-mail address: federica.belluti@unibo.it (F. Belluti).
[1] Department of Pharmaceutical Sciences, University of Piemonte Orientale, Largo Donegani 2, 28100 Novara, Italy.
[2] Aptuit, an Evotec Company, Via Alessandro Fleming 4, 37135 Verona, Italy.
[3] Department of Physics, University of Cagliari, S.P. Monserrato-Sestu Km 0,700, 09042 Monserrato (Cagliari), Italy.
[4] These authors contributed equally to this work.

https://doi.org/10.1016/j.ejmech.2023.115297
Received 30 January 2023; Received in revised form 15 March 2023; Accepted 16 March 2023
Available online 21 March 2023

It is increasingly accepted that a range of soluble Aβ assemblies, among which Aβ oligomers (AβOs), accumulate in the central nervous system (CNS): here, they exert a wide range of neurotoxic effects, not only at a molecular level but also via different mechanisms, such as oxidative and endoplasmic reticulum stress, mitochondrial dysfunction and membrane permeabilisation [4,5]. These effects are mutually involved in a feed-forward loop that ultimately leads to CNS cellular dysfunction and apoptosis, thus driving AD onset and progression [6]. AβOs and SPs, both directly or indirectly, trigger CNS inflammatory responses: they induce morphological changes in microglia and astrocytes responsible for the secretion of cytokines (interleukin-1β (IL-1β), interleukin-6 (IL-6), and tumour necrosis factor-α (TNF-α)), reactive oxygen species (ROS), and other cytotoxic elements [7]. In turn, these inflammatory mediators, highly expressed in the proximity of Aβ peptide deposits, enhance Aβ production and SPs deposition, and thus exacerbate neurodegeneration [8].

In response to stress and inflammatory conditions, the nuclear factor erythroid 2-related factor 2 (Nrf2) is released from its inhibitor Keap1, translocates into the nucleus, and, upon binding to the antioxidant response element, induces the transcription of antioxidant genes and the expression of a wide range of cytoprotective genes, among others NAD (P)H quinone oxidoreductase 1, heme oxygenase-1, superoxide dismutase (SOD), and catalase (CAT) [9,10]. Moreover, Nrf2 can directly regulate mitochondrial biogenesis and function, reducing the overproduction of intracellular ROS and the inflammatory response by inhibiting the activation of nuclear factor-kappa B and preventing the transcriptional upregulation of IL-6 and IL-1β [11].

In severely affected AD brains, the activities of antioxidant proteins like SOD, CAT, glutathione peroxidase (GPx), and glutathione reductase are remarkably upregulated; SOD activity, Nrf2 and total heme-oxygenase activity are similarly increased in moderately affected areas of the brain, whereas total GPx, CAT and peroxiredoxin activities are decreased [12]. Indeed, SOD1 and CAT represent first-line antioxidant enzymes that prevent or repair detrimental effects elicited by ROS and regulate redox-sensitive pathways in different species [13,14].

From this evidence, it emerges how the pathological state of AD consists of an arrangement of pathologic positive feedback loops, ultimately directing to a magnification of the original perturbation, and their concurrent modulation is becoming a helpful approach. Consequently, it is broadly recognised that the simultaneous modulation of different targets and interconnected pathways involved in multifactorial diseases, such as AD, represents a promising therapeutic approach [15]. Thus, as multifunctional agents promise improved effectiveness in comparison to single-target drugs [16,17], we identified the interconnected AβOs toxicity, neuroinflammatory and oxidative stress phenotypes as critical intervention points.

Natural products (NPs), regarded as precious sources of inspiration for drug design, offer a plethora of valuable molecular scaffolds and favoured ligand-protein binding motifs [18] from which structure-activity relationship studies can be performed. Among them, the polyphenol curcumin (**curc**, Fig. 1), found in the rhizome of *Curcuma longa*, has been demonstrated to feature a versatile opportunity in several therapeutic areas, especially neurodegeneration, cancer, and infectious diseases. In the AD framework, **curc** proved to hamper Aβ production and aggregation and to modulate a large variety of crucial targets and pathways, namely oxidative stress and neuroinflammation [19]. Extensive studies have investigated the molecular basis of **curc** anti-neurodegenerative effects. It emerged that the diarylhepta-1,4,6-trien-3-one function, containing an electron-rich α,β unsaturated carbonyl system, offers the opportunity to modulate several AD targets, likely by reacting *via* Michael's addition with cysteine residues. Recent modeling studies revealed that the binding of **curc** to Aβ42 and AβOs is governed by a proper balance between polar and hydrophobic interactions, mainly related to the ability of the side aryl rings to establish

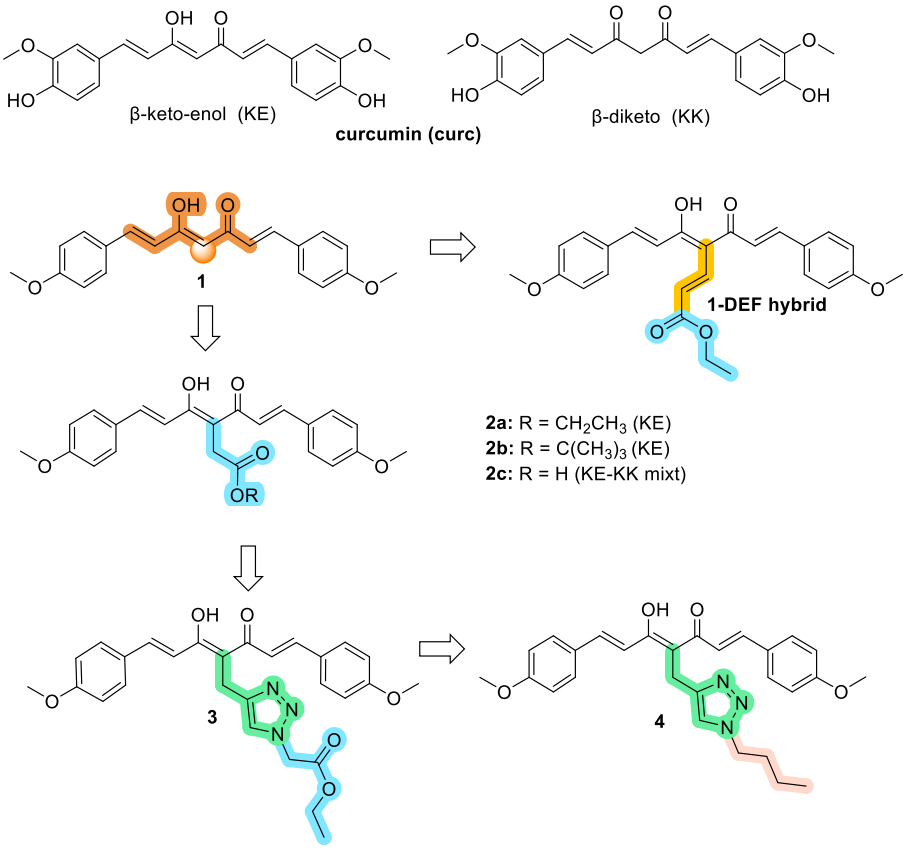

Fig. 1. Chemical structures of KE and KK **curc** tautomers, lead compound **1**, **1-DEF** hybrid, and design of the newly synthesised analogues **2a-c**, **3**, and **4**.

both H-bonds and π−π interactions [20].

Curc druggability has been subjected to debates in which some scientists defined it as a pan-assay interfering (PAIN) chemical and others as a discriminating agent [21–23]. Tailored modifications and functionalisation of the **curc** backbone successfully allowed for obtaining selective modulating agents for well-defined targets, thus demonstrating that compound's reactivity might be context-dependent [24]. In this arena, we and others have previously reported on different small libraries of **curc**-based analogues as therapeutic opportunities for modulating selected targets involved in neurodegenerative diseases [25–31].

2. Results and discussion

2.1. Design strategy

Curc, due to pleiotropic behaviour, proved to be a valuable lead compound to achieve stable, effective, selective, and non-toxic ligands for the modulation of anti-neurodegenerative relevant targets. In line with this, we previously discovered compound **1** (5-hydroxy-1,7-bis(4-methoxyphenyl)hepta-1,4,6-trien-3-one) as a dual inhibitor of the BACE-1 and GSK-3β, able to cross the blood brain barrier without eliciting CNS toxic effects [25]. The hybrid **1**-DEF (diethyl fumarate) was then developed by introducing an ethyl-acryloyl fragment into the 4-position of the central hepta-1,4,6-trien-3-one framework, obtaining a dual GSK-3β inhibitor/Nrf2 inducer [26].

In this study, as a continuation of our chemical exploration around lead **1**, some chemical modifications have been performed to obtain analogues with enlarged anti-AD potential (Fig. 1). In detail, the 4-position of hepta-1,4,6-trien-3-one core was decorated with an ester moiety, typically regarded as a versatile functional group in medicinal chemistry, leading to **2a** and **2b** as ethyl and *tert*-butyl functionalised derivatives, respectively; the corresponding carboxylic acid (**2c**) was also designed. Considering the detrimental role of the Aβ histidine (His13 and His14) in promoting amyloid aggregation through copper binding, the triazole heterocycle in **3** and **4** could hamper this His-driven process by interacting with these residues [32,33]. Thus, a 1,2,3-triazole heterocycle, regarded as a privileged fragment due to its attitude to make favourable interactions with biological macromolecules [34,35], was employed as a spacer. It was decorated with the ethyl ester moiety and an *n*-butyl group (compounds **3** and **4**, respectively) [36].

2.2. Synthesis

The synthetic strategy to obtain the curcumin-based analogues **2a-c**, **3**, and **4** is depicted in Scheme 1. First, intermediates **5**–**7**, obtained as mixtures of KE and KK tautomers, were synthesised by an alkylation reaction of pentane-2,4-dione with the suitable alkyl halide (ethyl-2-bromoacetate, *tert*-butyl 2-iodoacetate, or propargyl bromide, respectively) in the presence of a base [37].

Two different experimental conditions were employed: NaH and r.t. to obtain **5** and **6**, and anhydrous K_2CO_3 and heating to afford **7**. Then, a Pabon reaction [25,38,39] between these last intermediates and 4-methoxy benzaldehyde allowed obtaining the curcuminoids **2a**, **2b**, and **8** (KE form, in line with both ^{1}H NMR and ^{13}C NMR data). The saponification of the ethyl ester derivative **2a** using NaOH afforded the carboxylic acid derivative **2c** (KE-KK mixture). A Huisgen copper-catalysed alkyne-azide cycloaddition (CuAAC) [37] between the propargyl derivative **8** and the azides **9** and **10** (prepared by a reaction between the appropriate halides and NaN_3) gave **3** and **4** (KE/KK tautomeric couple and as KE tautomer, respectively).

2.3. Anti-inflammatory activity in microglial cells

2.3.1. Cell viability

Experiments to analyse **1**, **2a-c**, **3**, and **4** safety were first performed to identify a non-cytotoxic concentration range to ensure that any anti-inflammatory activity examined in the subsequent studies was specific to the compounds rather than a non-specific effect due to reduced cell viability. For this reason, cytotoxicity was initially screened by the 3-[4,5-dimethylthiazol-2-yl]-2,5 diphenyl tetrazolium bromide (MTT) assay on primary microglial cells, the resident immune cells of the CNS, which represent a powerful tool to test the potential anti-inflammatory effect of candidate compounds [40]. Compared to **curc** (used as a reference compound) [27,28,41], analogues **1**, **2a**, and **2c** exhibited lower cytotoxicity, considering that there was no effect on cell viability at concentrations ranging from 1 to 20 μM. The analogue **2b** exhibited similar cytotoxic impacts to those of **curc**, as it showed a significant decrease in microglia cell viability at 20 μM. Differently, compounds **3** and **4** markedly reduced microglia viability starting from the concentration of 10 and 5 μM, respectively (see Fig. S1).

2.3.2. Antiinflammatory activity

Following stimulation with lipopolysaccharide (LPS), the bacterial endotoxin most commonly used as a pro-inflammatory stimulus for

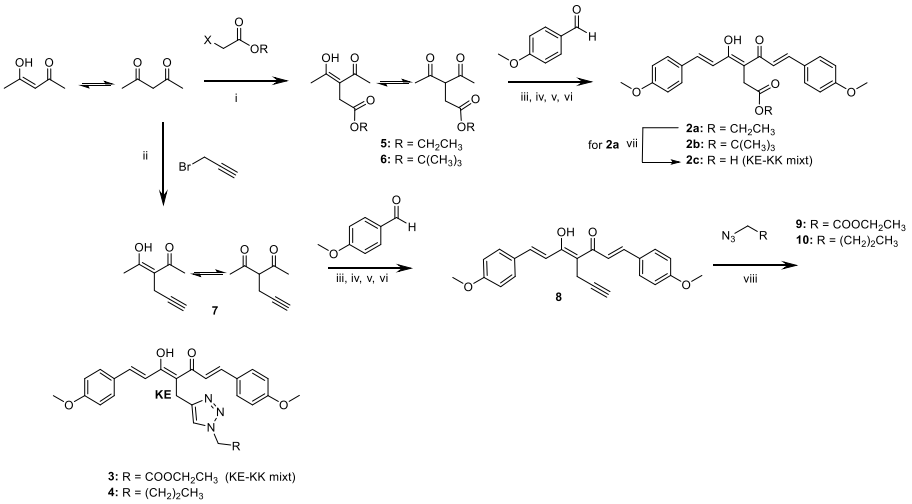

Scheme 1. Synthesis of the **curc**-derivatives **2a-c**, **3**, **4**. Reagents and conditions: i) Ethyl bromoacetate or *tert*-butyl 2-iodoacetate, NaH (60% dispersion in mineral oil), dry THF, N_2, 0 °C to r.t.; ii) propargyl bromide solution (80 wt % in toluene), anhydrous K_2CO_3, acetone, 80 °C; iii) B_2O_3, dry DMF; iv) B(*n*-BuO)$_3$; v) *n*-BuNH_2, 80 °C; vi) HCl, 80 °C; vii) NaOH (CH_3OH, 0.2 N), DCM/CH_3OH (9:1), r.t.; viii) $CuSO_4$, (+)-sodium L-ascorbate, DMF or DMSO, r.t.

immune cells [42], microglia secrete a variety of pro-inflammatory cytokines (TNF-α, IL-6, and IL-1β), chemokines and neurotoxic factors (ROS and nitrogen species), which result in neuronal insult and aggravate the progression of neurodegenerative diseases [43]. Accordingly, inhibiting the production of these mediators is an important therapeutic goal for developing anti-AD lead candidates. Microglia cells were exposed to increasing non-cytotoxic concentrations of compounds **1**, **2a-c**, **3**, and **4**, and **curc** (positive control) for 1 h and then stimulated with LPS for 24 h to induce the inflammatory response (Fig. 2). The anti-inflammatory effects were determined by measuring the compound's ability to inhibit the release of TNF-α and IL-1β, two master regulators of inflammation that are widely implicated in the pathogenesis of CNS disorders and share similar kinetics of release [44,45].

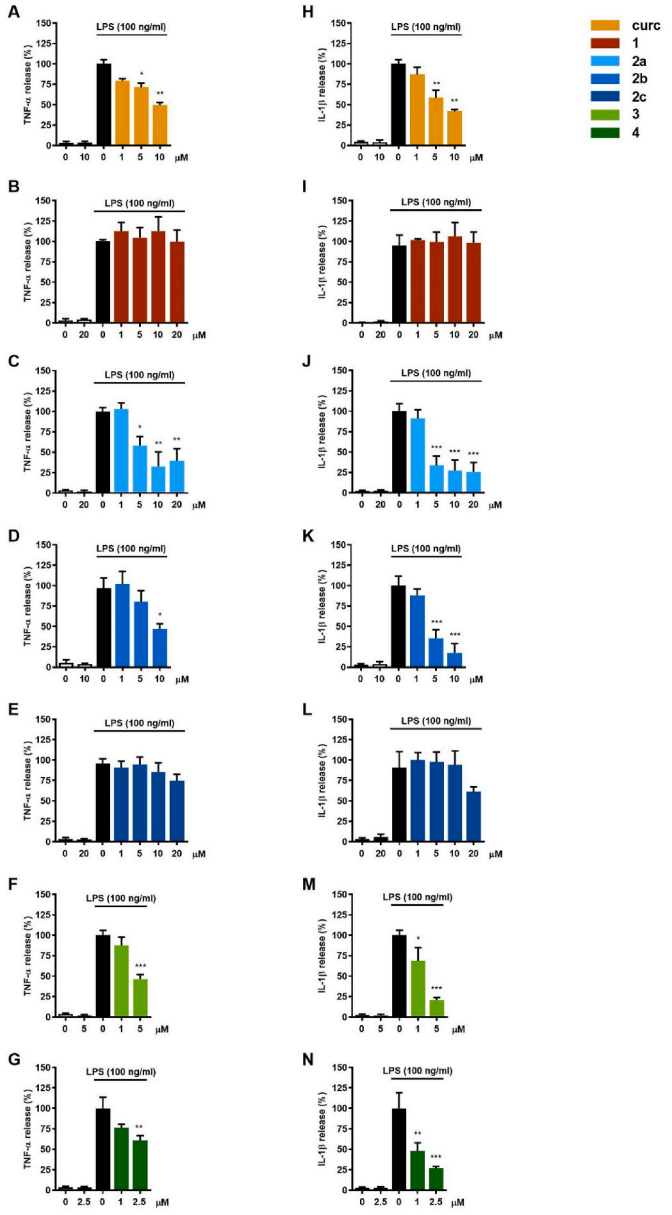

Fig. 2. Effects of **curc** and analogues **2a-c**, **3** and **4** on cytokine release from LPS-stimulated cortical microglia. Microglia were treated with the derivatives for 1 h and further stimulated with LPS. Supernatants were collected and analysed for TNF-α (**A-G**) and IL-1β (**H–N**) release. Results are expressed as a percentage of cytokine release relative to LPS-stimulated microglia (black bars). Data are reported as mean ± SEM of 3 independent experiments. *$p < 0.05$, **$p < 0.01$, and ***$p < 0.001$ *versus* LPS-stimulated cells. One-way ANOVA followed by Holm-Sidak's multiple comparison test.

Unstimulated cells released low or undetectable amounts of the above cytokines, which remained unchanged after treatment with the highest non-cytotoxic concentration of the compounds. On the contrary, LPS treatment markedly induced the release of TNF-α and IL-1β, which was significantly decreased by the newly synthesised analogues **2a**, **2b**, **3**, **4**, and by **curc**. In particular, derivatives **2a**, **2b,** and **3,** which bear an ester function (Fig. 2C, D, F, J, K, M), showed an inhibitory effect similar to that of **curc** (Fig. 2A, H); compound **4** bearing a triazole ring decorated with a lipophilic *n*-butyl chain, exerted the most remarkable anti-inflammatory effect, given that it strongly inhibited the release of TNF-α at the concentration of 2.5 μM and that of IL-1β starting from the final concentration of 1 μM (Fig. 2G, N). Surprisingly, lead compound **1** failed to inhibit the LPS-induced release of both cytokines at all the tested concentrations (Fig. 2B, I); the same effect was noticed for **2c**, characterised by a free carboxylic group (Fig. 2E, L).

The results from ELISA showing a robust anti-inflammatory activity for compounds **2a**, **3**, and **4** prompted us to perform further evaluations. Since Aβ aggregation has been shown to trigger upregulation and activation of the NLRP3 inflammasome, which, in turn, is involved in the cleavage of pro-IL-1β into the secreted form IL-1β [46], the mRNA levels of TNF-α and IL-1β, as well as those of the NLRP3, were measured.

Microglia cells were exposed to **2a** (10 μM), **3** (5 μM), and **4** (2.5 μM) and then stimulated with LPS; **curc** and **1** (10 μM) were used as the reference and negative control, respectively. Compounds **2a**, **3**, **4**, and **curc** markedly suppressed the LPS-induced increase of mRNA levels of the two cytokines and NLRP3, confirming the anti-inflammatory properties of the derivatives. Again, **1** demonstrated its inability to affect the microglial inflammatory response (Fig. 3A–C).

2.4. Antioxidant activity in human SH-SY5Y neuroblastoma cell line

2.4.1. Cell viability

As best performing in the microglia anti-inflammatory assay, the cytotoxicity of **1**, **2a**, **3**, and **4** was also evaluated in SH-SY5Y neuroblastoma cells [47].

Compounds **1** and **2a** did not show cytotoxicity at all the tested concentrations, while **3** and **4** recorded significant cytotoxicity at concentrations higher than 5 and 2.5 μM, respectively (see Fig. S2). As the above derivatives showed the same cytotoxicity profile observed in microglia cells (see Fig. S1), concentrations up to 2.5 μM were selected for the following experiments on this cell line.

2.4.2. Antioxidant activity

A decreased expression of Nrf2 was observed in neurons and glial cells of AD patients [10] with a concomitant reduction of the cytoprotective potential against cellular insults. Recent studies report that some NPs and NP-related molecules, such as **curc,** can exert indirect antioxidant effects and activate the Keap1/Nrf2 pathway resulting in transcriptional induction of glutathione (GSH) [48]. Based on these considerations, the SH-SY5Y intracellular GSH levels, after a 24 h treatment with analogues **1**, **2a**, **3**, and **4** at 2.5 μM, were determined by using the fluorescent probe monochlorobimane. A significant increase was observed for all tested analogues, and compound **4** resulted as the most active, with a percentage of around 40%. On the contrary, derivative **1** did not show any ability to amplify intracellular GSH (Fig. 4A).

Indirect antioxidant potential was investigated to determine whether the intensification of the total GSH level could translate into antioxidant effects. Cells were treated for 24 h with the selected compounds (2.5 μM) before adding the pro-oxidant *tert*-butyl hydroperoxide (*t*-BuOOH, 50 μM for 30 min), and ROS levels were measured by the fluorescent probe 2′,7′-dichlorodihydrofluorescein diacetate (H_2DCF-DA). The obtained results proved that only new compounds **2a**, **3**, and **4** reduced ROS formation with inhibition of around 38, 28 and 18%, respectively, while lead **1** did not elicit an indirect antioxidant effect (Fig. 4B).

To gain insight into the molecular basis of the increase in GSH, the activation of the Keap1/Nrf2 pathway was evaluated. SH-SY5Y cells

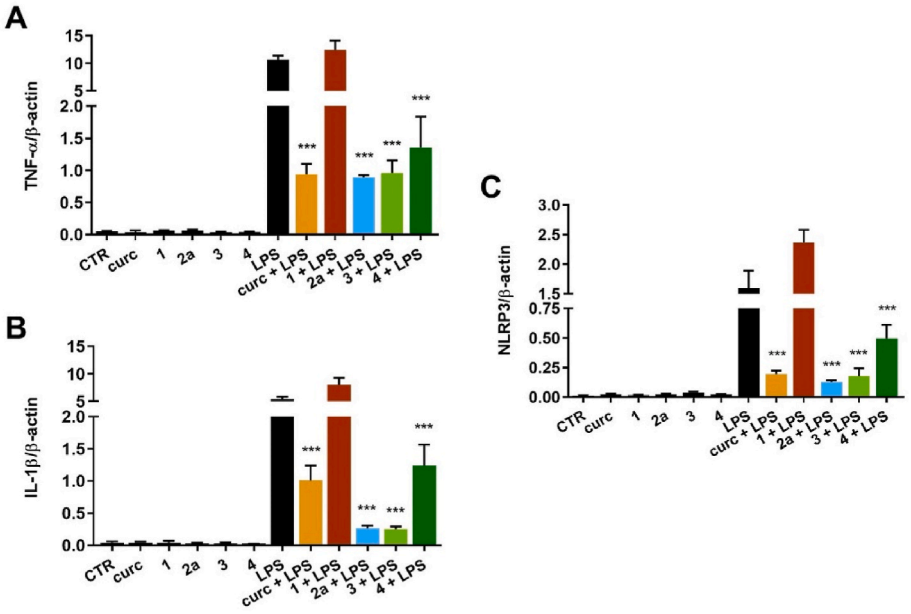

Fig. 3. Effect of **curc** and analogues on gene expression of inflammatory mediators in LPS-stimulated cortical microglia. Microglia were treated with the derivatives, followed by stimulation with LPS. (**A**) TNF-α, (**B**) IL-1β, and (**C**) NLRP3 mRNA levels were quantified by real-time PCR. Data are reported as mean ± SEM (n = 3 in triplicate). ***p < 0.001 versus LPS-stimulated cells. One-way ANOVA followed by Holm-Sidak's multiple comparison test.

were treated with compounds **1**, **2a**, **3**, and **4**, and nuclear and cytosolic Nrf2 levels were evaluated by Western blotting. Results are expressed as nuclear/cytosolic Nrf2 ratio, where an increased ratio indicates an enhancement of Nrf2 nuclear translocation. As shown in Fig. 4C, compounds **4** and **3**, but not **2a** and **1**, significantly induced Nrf2 nuclear translocation, suggesting that the triazole function plays a role in eliciting an indirect antioxidant effect.

2.5. Anti-oligomeric activity

In light of the anti-inflammatory and antioxidant properties described above for compounds **2a**, **3** and **4**, we next explored their anti-oligomeric activity using Aβ42 peptide. To this end, we exploited a well-established capillary electrophoresis (CE) assay that we first introduced in 2004 [49] and recently optimised [29,50]. By this method, the separation over time of non-toxic low molecular weight oligomers (LMW Aβ42Os) from toxic high molecular weight oligomers (HMW Aβ42Os) that build up in the capillary takes place in an aqueous buffer, to preserve the dynamic equilibrium of the non-covalent assemblies, before precipitation into fibrils [29,49]. Due to their heterogeneous and transient nature along the fibrillogenesis pathway, a debate is still ongoing on which oligomeric assemblies *in vivo* should be considered as the toxic pharmacological target [51]. Notably, the toxicity that we assigned to the HMW Aβ42Os separated by CE is supported by *in vivo* and *in vitro* data recently reported [29,52]. This CE method has already been widely used to monitor *in vitro* the anti-oligomeric effect of small molecules when these are added to the Aβ42 sample before analysis [27,29,53–56]. Here, as an initial screening, Aβ42 was coincubated with compounds **1**, **2a**, **3**, **4** and **curc** at the high non-cytotoxic concentrations reported for both microglia and SH-5YSY cells (Figs. S1 and S2). Fig. S3 clearly shows that all compounds but **1** and **2a** are endowed with anti-oligomeric activity when compared to control with the following ranking: **4** > **3** > **curc**. In detail, the most striking effect was exerted by **4**, as its presence completely depleted the formation of toxic HMW Aβ42Os after two days from sample solubilisation. This high activity, for up to ten days, was observed for the first time at these concentrations [27,29,53–55]. Compound **3** also showed a remarkable anti-oligomeric activity, higher than that of **curc**. As both **4** and **3** bear a triazole ring, it is suggested that the *n*-butyl lipophilic chain would make a difference in hampering the peptide-peptide interaction, similarly to what reported above for the anti-inflammatory activity. Lead **1** and analogue **2a** showed a clear pro-aggregating property. Consequently, it can be derived that the triazole function is likely to be crucial for the activity.

To better understand how data from Fig. S3 were retrieved, Fig. 5 reports the electropherograms of this screening, taken at day 7 from solubilisation: here, it can also be appreciated that, conversely to **1** and **2a**, while the active compounds reduce the toxic HMW Aβ42Os to a different extent, they also perturb the formation kinetics of oligomers by keeping the LMW Aβ42Os stable in solution.

These encouraging findings prompted us to investigate a concentration as low as 1 μM of **3** and **4**, using **1** and **curc** as negative control and reference, respectively. After 7 days from solubilisation, the activity of **3** and **4** levels off at similar values and is still very high, especially if compared with that of **curc** (Fig. 6). After 10 days from solubilisation it becomes clear how a complete or almost complete depletion of HMW Aβ42Os is induced by compound **4** and **3**, respectively (Fig. 6 and electropherograms in Fig. S4). By comparing this behaviour for compound **4** (1 μM) with data in Fig. S3 (2.5 μM), a time and concentration dependent activity can be derived. It seems like compound **4** would even catalyze prompt oligomerisation of Aβ42 monomers into oligomers, which further on disaggregate. We have already observed this initial presence of oligomers, at different extent, both in absence and presence of small molecules and the disaggregation/stabilisation effect of, e.g. mitoxantrone [53] or of a bis-tacrine derivative [54] as well as of other curcumin derivatives [29]. Nevertheless, the complete depletion of HMW Aβ42 by a small molecule at a concentration as low as 1 μM is observed here for the first time. We already thoroughly demonstrated that the LMW Aβ42Os here left in solution, unlike HMW Aβ42Os, do not affect SH-SY5Y and microglia viability [29,50], do not enhance the release of inflammatory cytokines and leave primary cortical neurons intact upon treatment [29].

Therefore, the anti-oligomeric profile of **3** and **4** also translates into reduced toxicity and this makes them the most active **curc**-based derivatives that we have tested so far [27,29].

2.6. Computational studies

Given the striking differences observed in the anti-aggregation

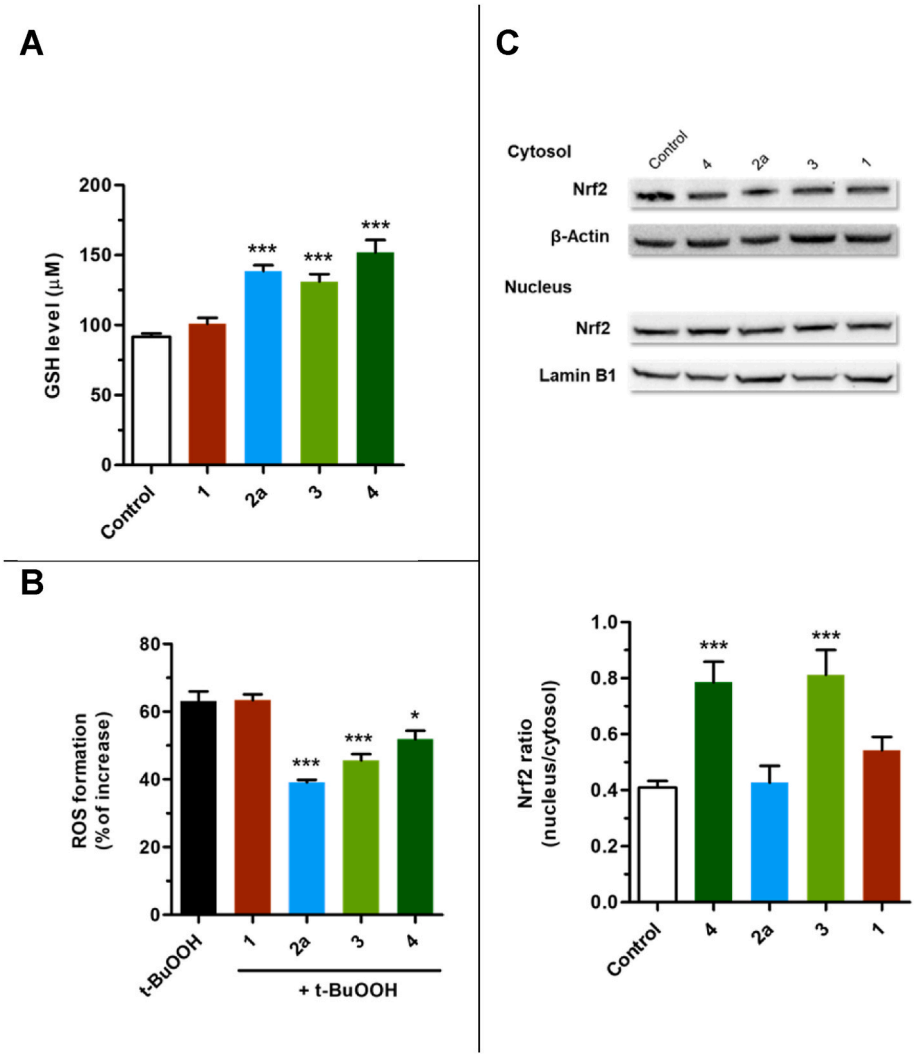

Fig. 4. Indirect antioxidant activity of **curc** analogues (2.5 μM of **1, 2a, 3** and **4**) in SH-SY5Y cells. (**A**) Cells were treated for 24 h with the **curc** analogues to evaluate GSH; (**B**) cells were treated for 24 h with the **curc** analogues before adding the pro-oxidant *tert*-butyl hydroperoxide (50 μM) to evaluate ROS; (**C**) cells were treated for 3 h with the **cur** analogues to evaluate Nrf2 translocation levels. Data are reported as mean ± SEM of three independent experiments. (**A**)***p < 0.001 versus untreated cells; (**B**) *p < 0.05 and ***p < 0.001 versus cells treated with *t*-BuOOH; (**C**) ***p < 0.001 versus untreated cells. One-way ANOVA with Dunnett's Post Hoc Test.

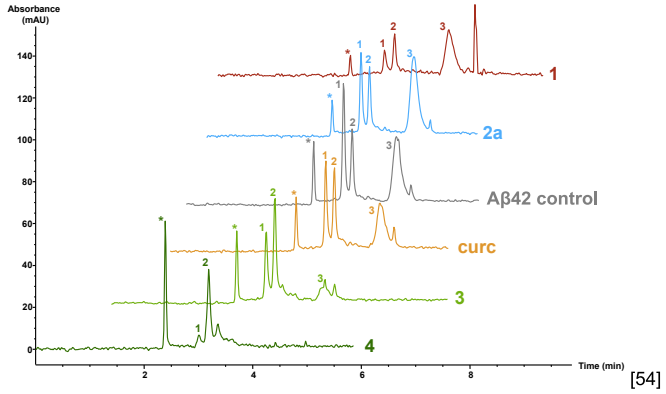

[54]

Fig. 5. Electrophoretic profiles of 221 μM Aβ42 control and 221 μM Aβ42 control in the presence of 5 μM **curc**, **1**, **3** and 2.5 μM **4**. Peak * refers to the electroosmotic flow. Peaks 1 and 2 are related to the migration of non-toxic LMW Aβ42Os (from trimers up to dodecamers), while peak 3 is related to the migration of toxic HMW Aβ42Os (aggregates smaller than 22-mers and larger than dodecamers) [29,50]. Electropherograms are taken at 7 days from sample dissolution.

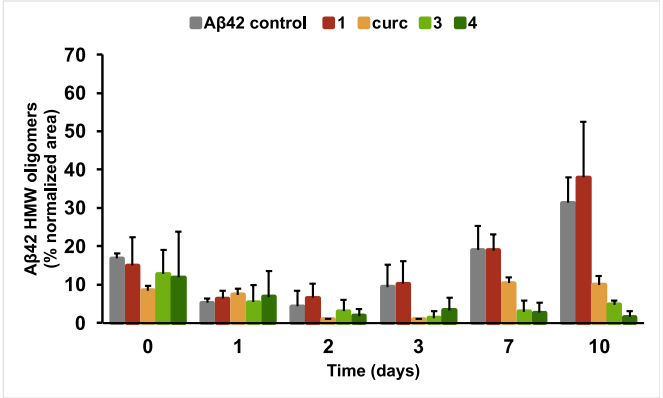

Fig. 6. Effect of **curc** and **curc**-based analogues **1**, **3**, and **4** on Aβ42 oligomerisation. Normalised area percentage plots of toxic HMW Aβ42Os from a 221 μM solution of Aβ42 monomer, in the absence (Aβ42 control) and in the presence of 1 μM **curc**, **1**, **3** and **4**. Data are expressed as mean ± standard deviation (n = 3).

activity of the newly synthesised **curc**-analogues, docking studies were performed to verify whether the depletion of HMW Aβ42Os is reflected in the interaction with the Aβ fibril at a molecular level. In detail, blind docking simulations were carried out on multiple NMR structures of the

Aβ fibril, and the overall distribution of the docking poses along the fibril was investigated [57].

Fig. 7 shows the six main hotspots found by clustering all the docking poses (see Experimental Section). The six spots are distributed in different regions of the fibril: Spot1 is located near the *N*-terminal, where compounds can interact with the fibril through hydrogen bonds, mainly with Glu11 and His13 (Fig. S5A). Spot2 was found to be important in previous studies, pointing to the role of His14 and Lys16 (Fig. S5B) [58]. Spot3 is defined by a hydrophobic (Val18) and a negatively charged (Glu22) site (Fig. S5C), while Spot4 is mainly polar (Ser26 and Lys28, Fig. S5D) and should be involved in a salt bridge with the *C*-terminus. Spot5 (Fig. S5E) and Spot6 are mostly lined by apolar residues: Leu17, Ile32 and Leu34 in Spot5, Val39, and Val40 in Spot6.

Table 1 reports the cluster population and the weighted score associated with each spot. Although all compounds were found in the six hotspots, the docking scores for each region show differences, which allow for some relevant considerations.

Firstly, compounds **3** and **4** reached the best scores in all the spots. Moreover, the better scores shown by these compounds compared to **curc** are in agreement with their higher anti-oligomeric activity. Secondly, the comparison between the scores as derived for Spots1 and Spot2 can provide helpful insights to rationalise better the pro-aggregating effect elicited by **2a**. Although all compounds reached higher scores in Spot1 than in Spot2 (indicating that the **curc**-based portion is suitable for interacting with Aβ and could likely act as an anchoring fragment), the pro-aggregating compound **2a** reveals the largest difference between the two binding sites, which suggests that it binds almost exclusively Spot1. In contrast, compounds **3** and **4** showed remarkable scores for all spots, including Spot2, whose anti-aggregating role was already described.

Taken together, docking results indicate that the propensity of compounds to bind within the central regions of the fibril prevents its assembly, while compounds that preferentially bind in the peripheral regions of the fibril facilitate its elongation. This behaviour would imply that **3** and **4** are among those compounds that inhibit both oligomerisation and fibrillisation [59].

2.7. Antioxidant activity in Drosophila model

Animal models allow the understanding of the underlying molecular basis of a bioactive compound, along with conducting the preclinical screening. Particularly, since the beginning of the 20th century, the tiny fruit fly, *Drosophila melanogaster,* has been regarded as a valuable model organism for several human disorders, among others affecting CNS.

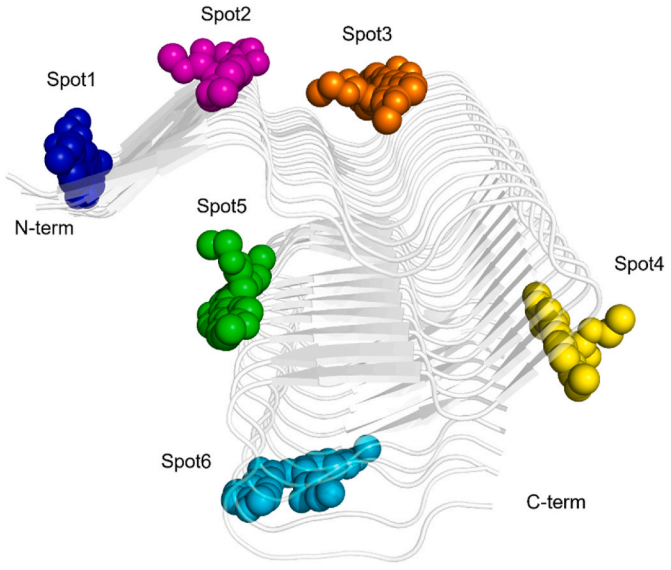

Fig. 7. Localisation of the six main clusters on the Aβ42 fibril. Cluster 1 is reported in blue, 2 in magenta, 3 in orange, 4 in yellow, 5 in green and 6 in cyan.

Table 1
Weighted docking scores (kcal/mol) of the ligands associated with the six hot spots.

	Spot1	Spot2	Spot3	Spot4	Spot5	Spot6	Mean
Curc	−60.7	−52.4	−55.8	−62.6	−62.2	−52.8	−57.8
1	−62.4	−59.0	−55.4	−60.0	−63.2	−55.7	−59.3
2a	−66.2	−55.3	−55.1	−64.9	−66.1	−56.6	−60.7
3	−72.6	−68.5	−64.1	−68.2	−72.5	−64.6	−68.4
4	−76.1	−66.9	−62.0	−68.7	−71.9	−68.8	−69.1

Based on the data obtained, **3** and **4** were selected to be studied for their *in vivo* antioxidant effects in *Drosophila* models by evaluating ROS level and expression of Nrf2, SOD1, and CAT on neuronal and non-neuronal tissues.

2.7.1. Toxicity analysis

Compounds **3** and **4** were tested *in vivo* on the control *Drosophila* line to identify the most effective and non-toxic concentration range [60]. Then a second experiment was carried out to identify the concentration that allowed the correct development of *Drosophila* into the adult stage (see Table S1). The parameters evaluated were the development time from larva to adult, the number of pupae per tube and the number of successfully eclosed flies. The most effective concentration with minimal toxic effects was determined to be 10 μM (see Fig. S6) and was chosen for the subsequent antioxidant activity assays.

2.7.2. In vivo effects in Drosophila neurodegenerative model: oxidative stress evaluation

From observing the *in vitro* antioxidant profiling of the set of new compounds, triazole-based **3** and **4** emerged as the most interesting. *In vivo* proof-of-concept studies were performed to deeper assess their antioxidant potentials, such as evaluation in larval tissues and adults of control and Spastin *Drosophila* model. Cartoons depict dissected third instar larvae showing the muscle schematic organisation in the abdominal segments A1-7 (Fig. 8) and in the brain (Fig. 9), where the experiments were conducted. The images of larval muscles and the brain of the control treated with compounds are reported in Fig. S7. Genetic reduction or depletion of Spastin was reported to cause cellular stress in neuronal and non-neuronal tissues in different *in vivo* and *in vitro* models [61–63].

The *in vivo* intracellular ROS levels were quantified in larval muscle tissues and brains (Figs. 8 and 9) using DHE, a redox-sensitive and cell-penetrating fluorogenic probe that exhibits increased fluorescence intensity when oxidised by intracellular ROS [64], the blue-fluorescent DNA stain DAPI was employed to visualise nuclei. DHE-assay showed that ROS levels increased in larval muscles and brains under neurodegenerative conditions (D-spastin loss of function model), in line with the cellular stress produced by the reduction of D-spastin [61,62]. When tested on the D-spastin model, compound **3** slightly decreased ROS levels; interestingly, compound **4** efficiently restored the ROS level to that observed for the control.

To gain insight into the mechanism of action of the selected curcuminoids, we tested whether changes in ROS levels were mediated by Nrf2. For this purpose, we evaluated the expression levels of Nrf2 transcript in treated and untreated *Drosophila* (neurodegenerative Spastin model and control). Nrf2 transcript expression was significantly upregulated in the Spastin model, and the treatment with compounds **3** or **4** (Fig. 10A) significantly ameliorates the phenotype associated with spastin reduction.

The increased stationary ROS levels in spastin mutant could be due to altered expression/activity of antioxidant enzymes required for ROS scavengings, such as CAT or SOD1. To test this hypothesis, in animals

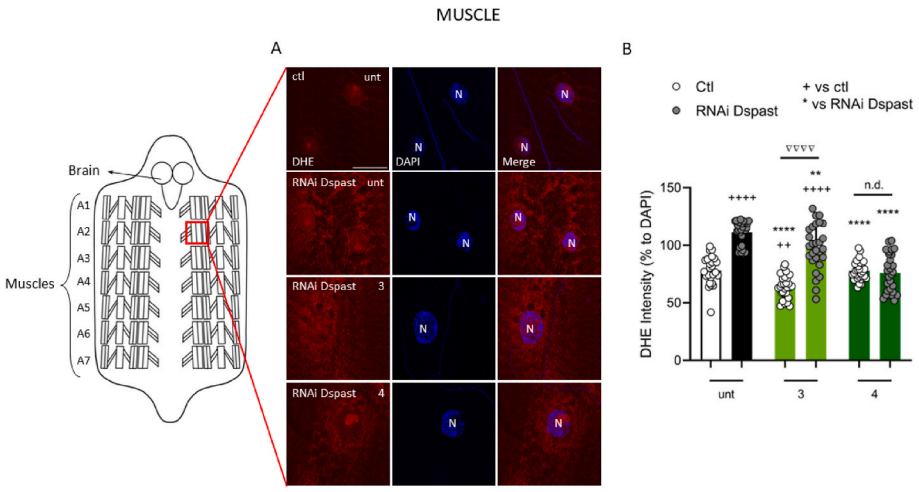

Fig. 8. Effects of compounds **3** and **4** on muscle ROS levels in Spastin *Drosophila* model. The red square indicates the A2 muscles that were acquired and analysed. (**A**) Control line (*Tubulin-Gal4/+)* and Spastin *Drosophila* (*Tubulin-Gal4/RNAiDSpast*) line were raised in standard and **3** or **4** enriched food. Dissected larvae were stained with DHE to detect ROS levels (red) and DAPI to visualise nuclei (blue). Scale bar = 20 μm. (**B**) The graph shows the relative intensity of DHE with respect to DAPI intensity in larval muscles (one-way ANOVA with Tukey's post hoc test; n > 13 larvae; * vs RNAi Dspast/Tub; + vs Tub/+).

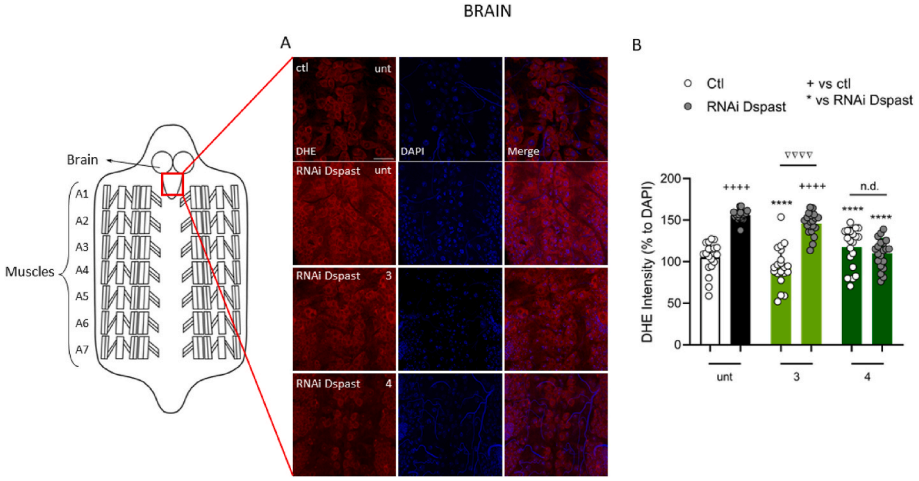

Fig. 9. Effect of compounds **3** and **4** on brain ROS levels in Spastin *Drosophila* model. The red square indicates the brain portion that was acquired and analysed. (**A**) Control line (*Tubulin-Gal4/+*) and Spastin *Drosophila* line (*Tubulin-Gal4/RNAiDspast*) were raised in standard and **3** or **4** enriched food. Dissected larvae were stained with DHE to detect ROS levels (red) and DAPI to visualise nuclei (blue). Scale bar = 20 μm. (**B**) The graph shows the relative intensity of DHE with respect to DAPI intensity in larval muscles (one-way ANOVA with Tukey's *post hoc* test; n > 13 larvae; * vs RNAi Dspast/Tub; + vs Tub/+).

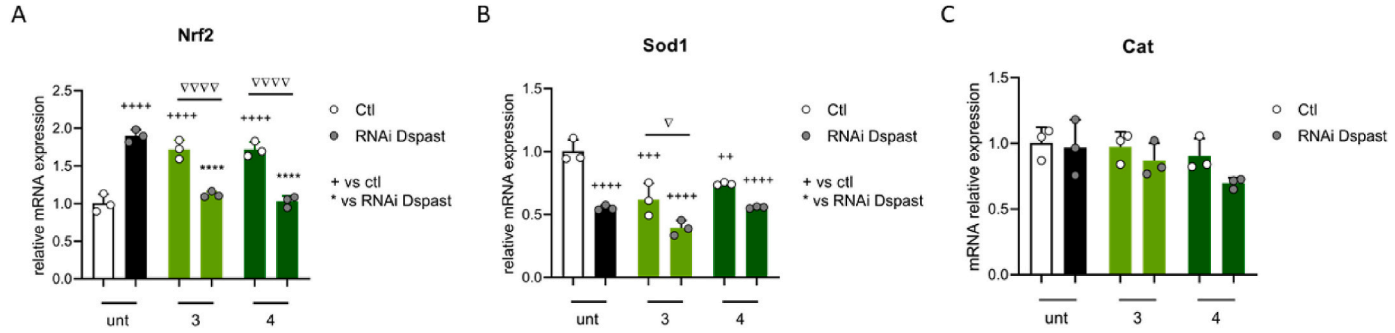

Fig. 10. Expression levels of Nrf2 (**A**), SOD1 (**B**) and CAT (**C**) in Spastin *Drosophila* line. The RNA was extracted from larvae raised in standard food and **3** or **4** enriched medium. *Tubulin-Gal4/+* line (Tub/+) was used as control. Results are expressed as individual data plus mean ± SEM (one-way ANOVA with Tukey's *post hoc* test; n = 3 experiments; * vs RNAi Dspast/Tub; + vs Tub/+).

treated with **3** and **4**, the transcriptional level of SOD1 and CAT were measured (Fig. 10B and C, respectively). Regarding CAT, no difference was observed among samples; on the contrary, SOD1 expression level was downregulated in spastin mutant and control samples, suggesting that administration of the compounds negatively modulates SOD1 expression and was unable to restore the phenotype of Spastin model.

In summary, from the *in vivo* proof-of-concept studies, it emerged how the obtained data from the different models generally confirmed conserved mechanisms for both compounds. In particular, the marked ROS levels reduction obtained by treatment with compound **4** was the consequence of the modulation of redox-sensitive signalling pathways, namely Nrf2 and the interconnected SOD1 enzyme.

3. Conclusion

To tackle the complex AD pathology, a small series of **curc**-based analogues, as potential multifunctional ligands, was designed to specifically target neuroinflammation and oxidative stress as crucial

aspects, sharing Aβ aggregation triggering event. The bioactivity profile of the new analogues was assessed through an assay pipeline in different cell environments from which **2a**, **3** and **4** showed favourable anti-inflammatory and antioxidant effects in terms of decrease of pro-inflammatory cytokine release from microglia and induction of Nrf2 from SH-SY5Y cells. Among them, the triazole-based **3** and **4** effectively suppressed toxic HMW AβOs formation, likely due to positive interactions of the triazole function with crucial Aβ residues, among others, His13 and His14.

In summary, by *in vitro* data, analogue **4**, with an *n*-butyl substituent on the triazole and prevalently in the KE-tautomer conformation, performed better than **3**, with an ester function and as a KE-KK mixture. Indeed, a coplanar "flat" conformation of a KE-curcuminoid scaffold, also characterised by an extended conjugation, has been found to be a favourable structural requirement for several bioactivities, among which Aβ interaction [65].

Yet again, when tested in an *in vivo* oxidative stress model, analogue **4** proved to perform better than **3**, as it efficiently restored ROS level and modulated the antioxidant enzyme SOD1 without eliciting toxic effects.

In conclusion, our results lie in finding the multipotent activity profiles of the tailored functionalised **curc**-analogues **3** and **4** that, owing to the anti-inflammatory, antioxidant, and anti-oligomerisation effects, could offer promise in fronting the multifaceted AD toxicity. In particular, compound **4**, showed remarkable neuroprotective activity and emerged as a potential anti-AD lead candidate.

4. Experimental Section

4.1. Chemistry

4.1.1. General chemistry information

Chemical reagents and solvents, unless otherwise specified, were employed as commercial products with a high-grade purity. Reaction courses were monitored by thin-layer chromatography (TLC) performed on precoated TLC plates (Merck Silica Gel 60 F254, layer 0.20 mm) and then visualised under a UV lamp (λ = 254 and 365 nm). Chromatographic separations were performed on silica gel columns using the flash method (Kiesegel 40, particle size 0.040–0.063 mm, Merck). Melting points were determined in open glass capillaries using a Büchi apparatus and were uncorrected. ^{1}H NMR and ^{13}C NMR spectra were recorded on a Varian INOVA spectrometer operating at 400 MHz and 101 MHz, respectively; data are reported as follows: chemical shift (ppm δ value), multiplicity (indicated as: br., broad signal; s, singlet; d, doublet; t, triplet; q, quartet; p, quintet; m, multiplet and combinations thereof), coupling constants (*J*) in Hertz (Hz) and integrated intensity. Mass spectra were recorded on a Waters ZQ 4000 apparatus operating in electrospray mode (ES). ESI HRMS spectra were recorded on a Waters Q Tof apparatus. UHPLC−MS analyses were run on a Waters ACQUITY ARC UHPLC/MS system consisting of a QDA mass spectrometer equipped with an electrospray ionisation interface and a 2489 UV/Vis detector; the detected wavelength was 365 nm. Analyses were performed on an XBridge BEH C18 column (10 × 2.1 mm i.d., particle size 2.5 μm) with an XBridge BEH C18 VanGuard Cartridge precolumn (5 mm × 2.1 mm i.d., particle size 1.8 μm); the mobile phases were H_2O (0.1% formic acid) (A) and MeCN (0.1% formic acid) (B). Linear gradient: 0−0.78 min, 20% B; 0.78–2.87 min, 20−95% B; 2.87–3.54 min, 95% B; 3.54–3.65 min, 95-20% B; 3.65-5-73, 20% B. Flow rate: 0.8 mL/min. Electrospray ionisation in positive and negative modes was applied in the mass scan range of 50–1200 Da. All tested compounds were found to have >95% purity. FT-IR spectra were recorded on Bruker Apha FT-IR, Platinum ATR with monolithic diamond Crystal. The compound's name is in accord with the naming algorithm developed by CambridgeSoft Corporation and used in Chem-BioDraw Ultra 20.1.

4.1.2. General Procedure A (Pabon reaction, compounds **2a** and **2b**, and **8**)

To a suspension of alkylated pentane-2,4-dione (**5**, **6** or **7**, 1.00 mmol) and B_2O_3 (1.0 molar equiv) in dry DMF (1.5 mL), stirred for 30 min at 80 °C, B(*n*-BuO)$_3$ (4.0 molar equiv) was added, and the resulting mixture was heated for additional 30 min. Then, the sequential addition of 4-methoxy benzaldehyde (1.8 molar equiv) and a solution of *n*-BuNH$_2$ (0.4 molar equiv) in dry DMF (1.0 mL) was carried out. After stirring at 80 °C for 8–10 h, the resulting solution was cooled to r.t., acidified with aqueous 0.5 N HCl solution (8 mL) and stirred at 80 °C for 30 min. The obtained precipitate was filtered and purified by flash column chromatography (FCC) using a mixture of PE/EtOAc as eluent and then crystallised with a suitable solvent. The synthesised compounds were structurally characterised (mono and bi-dimensional NMR experiments) to assess their tautomeric form along with the *E* configuration of the C═C double bonds.

*4.1.2.1. Ethyl (3Z,5E)-4-hydroxy-6-(4-methoxyphenyl)-3-((E)-3-(4-methoxyphenyl)acryloyl) hexa-3,5-dienoate (**2a**-KE).* Starting from **5** (KE/KK mixture,1.00 g, 5.37 mmol) and 4-methoxy benzaldehyde (1.17 mL, 9.67 mmol), a crude product was obtained, which was purified by FCC (PE/EtOAc, 8:2) and crystallised from a DCM/PE mixture to afford the title compound as a red solid (60% yield, mp 125–127 °C). ^{1}H NMR ($CDCl_3$): δ 1.26 (t, 3H, *J* = 7.0 Hz, $OCH_2\underline{CH_3}$), 3.56 (s, 2H, $\underline{CH_2}COOCH_2CH_3$), 3.86 (s, 6H, OCH_3), 4.20 (q, 2H, *J* = 6.8 Hz, $O\underline{CH_2}CH_3$), 6.93 (d, 4H, *J* = 8.8 Hz, Ar), 7.05 (d, 2H, *J* = 15.2 Hz, CO-$\underline{CH}\alpha$=CHβ), 7.55 (d, 4H, *J* = 8.8 Hz, Ar), 7.75 (d, 2H, *J* = 15.4 Hz, CO-CHα=$\underline{CH}\beta$). ^{13}C NMR ($CDCl_3$): δ 14.4 ($OCH_2\underline{CH_3}$), 32.4 (CH_2), 55.5 (2C, OCH_3), 61.3 ($O\underline{CH_2}CH_3$), 104.7 (CO–$\underline{C}(CH_2COOEt)$=COH), 114.5 (4C, CH-Ar), 118.4 (2C, CO-$\underline{CH}\alpha$=CHβ), 128.3 (2C, Cq-Ar), 130.1 (4C, CH-Ar), 142.1 (2C, CO-CHα=$\underline{CH}\beta$), 161.5 (2C, Cq-Ar), 171.9 (CO), 183.7 (2C, CO and =COH). See Fig. S8 for ^{1}H NMR and ^{13}C NMR spectra. Formula: $C_{25}H_{26}O_6$, MW: 422.48, ESI-MS (*m/z*): 445 (M+Na). HRMS *m/z*: [M+Na]: calcd. for $C_{25}H_{26}NaO_6$ 445.1621; found 445.1600. FT-IR (ATR, υ) cm^{-1} 1732, 1596, 1508, 1423, 1299, 1250, 1163, 1020, 968, 820, 517. Purity 100% (UPLC/MS). See Fig. S13 for RP-UPLC/MS chromatogram.

*4.1.2.2. tert-Butyl (3Z,5E)-4-hydroxy-6-(4-methoxyphenyl)-3-((E)-3-(4-methoxyphenyl)acryloyl) hexa-3,5-dienoate (**2b**-KE).* Starting from **6** (KE/KK mixture, 0.27 g, 1.26 mmol) and 4-methoxy benzaldehyde (0.28 mL, 2.27 mmol), a crude product was obtained, which was purified by FCC (PE/EtOAc, 8.5:1.5) and crystallised from DCM/PE mixture to afford the title compound as an orange-yellow solid (73% yield, mp 154–156 °C). ^{1}H NMR ($CDCl_3$): δ 1.45 (s, 9H, $O\underline{C(CH_3)_3}$), 3.47 (s, 2H, $\underline{CH_2}COOC(CH_3)_3$), 3.86 (s, 6H, OCH_3), 6.93 (d, 4H, *J* = 8.8 Hz, Ar), 7.08 (d, 2H, *J* = 15.4 Hz, CO-$\underline{CH}\alpha$=CHβ), 7.56 (d, 4H, *J* = 8.7 Hz, Ar), 7.74 (d, 2H, *J* = 15.4 Hz, CO-CHα=$\underline{CH}\beta$). ^{13}C NMR ($CDCl_3$): δ 28.2 (3C, OC$\underline{(CH_3)_3}$), 33.7 (CH_2), 55.5 (2C, OCH_3), 81.5 ($O\underline{C}(CH_3)_3$), 105.3 (CO–$\underline{C}(CH_2COOt\text{-}Bu)$=COH), 114.5 (4C, CH-Ar), 118.7 (2C, CO-$\underline{CH}\alpha$=CHβ), 128.4 (2C, Cq-Ar), 130.1 (4C, CH-Ar), 141.7 (2C, CO-CHα=$\underline{CH}\beta$), 161.5 (2C, Cq-Ar), 171.2 (CO), 183.7 (2C, CO and =COH). Formula: $C_{27}H_{30}O_6$, MW: 450.53, ESI-MS (*m/z*): 473 (M+Na). HRMS *m/z*: [M+Na]: calcd. for $C_{27}H_{30}NaO_6$ 473.1935, found: 473.1918. FT-IR (ATR, υ) cm^{-1} 2918, 1724, 1600, 1511, 1423, 1309, 1248, 1142, 1027, 975, 817, 517. Purity 97.31% (UPLC/MS). See Fig. S13 for RP-UPLC/MS chromatogram.

*4.1.2.3. (1E,4Z,6E)-5-hydroxy-1,7-bis(4-methoxyphenyl)-4-(prop-2-yn-1-yl)hepta-1,4,6-trien-3-one (**8**-KE).* Starting from **7** (KE/KK mixture, 1.41 g, 10.20 mmol) and 4-methoxy benzaldehyde (2.23 mL, 18.36 mmol), a crude product was obtained, which was purified by FCC (PE/EtOAc, 8.5:1.5) to afford the title compound as **8** as yellowish solid (52% yield, mp 135–137 °C). ^{1}H NMR ($CDCl_3$): δ 2.15 (t, 1H, *J* = 2.4 Hz, $CH_2C\underline{CH}$), 3.44 (d, 2H, *J* = 2.4 Hz, $\underline{CH_2}CCH$), 3.87 (s, 6H, OCH_3), 6.94 (d, 4H, *J* = 8.4 Hz, Ar), 7.04 (d, 2H, *J* = 15.2 Hz, CO-$\underline{CH}\alpha$=CHβ), 7.58 (d, 4H, *J* =

8.8 Hz, Ar), 7.77 (d, 2H, J = 15.2 Hz, CO-CHα=CHβ). ^{13}C NMR ($CDCl_3$): δ 16.22 (CH_2CCH), 55.38 (2C, OCH), 69.58 (CCH), 82.54 (CH_2CCH), 106.28 (CO–C(CH_2CCH)=COH), 114.38 (4C, CH-Ar), 117.93 (2C, CO-CHα=CHβ), 128.07 (2C, Cq-Ar), 130.01 (4C, CH-Ar), 141.92 (2C, CO-CHα=CHβ), 161.39 (2C, Cq-Ar), 182.71 (CO and =COH). HRMS *m/z*: [M+Na]: calcd. for $C_{24}H_{22}NaO_4$, 397.1416; found 397.1411. FT-IR (ATR, υ) cm^{-1} 1592, 1609, 1249, 1168, 1025, 975, 821, 514

*4.1.3. (3Z,5E)-4-hydroxy-6-(4-methoxyphenyl)-3-((E)-3-(4-methoxyphenyl)acryloyl)hexa-3,5-dienoic acid (**2c**-KE) and (E)-6-(4-methoxyphenyl)-3-((E)-3-(4-methoxyphenyl)acryloyl)-4-oxohex-5-enoic acid (**2c**-KK)*

A 0.2 N NaOH solution in MeOH (19 mL) was added for 30 min to a solution of **2a** (0.80 g, 1.89 mmol) in DCM/MeOH (9:1, 4 mL), and the resulting mixture was allowed to stir at r.t. for 1 h. The organic solvent was evaporated under reduced pressure, and the aqueous phase was washed twice with Et_2O (2 × 15 mL) and then acidified with aqueous HCl solution (6 N) until precipitation of a solid, which was filtered. The isolate crude product was then treated with a DCM/PE mixture, and a final crystallization of the obtained solid with EtOH gave the desired compound as a pale brown solid (2.2:1.0 mixture of KE/KK, 75% yield, mp 147–149 °C). ^{1}H NMR ($CDCl_3$): δ 2.77 (d, 2H, J = 6.8 Hz, CH_2COOH, KK), 3.03 (t, 1H, J = 6.4 Hz, CH, KK), 3.77 (s, 2H, CH_2COOH, KE), 3.86 (s, 12H, OCH_3, KE + KK), 6.32 (d, 2H, J = 16.4 Hz, CO-CHα=CHβ, KE), 6.67 (d, 2H, J = 16.4 Hz, CO-CHα=CHβ, KK), 6.93 (d, 8H, J = 8.4 Hz, Ar, KE + KK), 7.51 (d, 4H, J = 7.6 Hz, Ar, KE), 7.52 (d, 4H, J = 7.6 Hz, Ar, KK), 7.59 (d, 2H, J = 16.4 Hz, CO-CHα=CHβ, KK), 7.73 (d, 2H, J = 16.4 Hz, CO-CHα=CHβ, KE). ^{13}C NMR ($CDCl_3$) δ 28.2 (CH_2), 35.0 (CH_2), 55.5 (5C, OCH_3 and COCHCH$_2$COOHCO), 114.5 (4C, CH-Ar), 114.6 (4C, CH-Ar), 114.7 (CO–C(CH_2COOH)=COH), 123.6 (4C, CO-CHα=CHβ), 126.9 (2C, Cq-Ar), 127.1 (2C, Cq-Ar), 130.2 (8C, CH-Ar), 143.2 (2C, CO-CHα=CHβ), 146.9 (2C, CO-CHα=CHβ), 161.8 (2C, Cq-Ar), 161.9 (2C, Cq-Ar), 172.6 (2C, CO), 178.7 (2C, CO), 198.0 (2C, CO and =COH). Formula: $C_{23}H_{22}O_6$, MW: 394.42, ESI-MS (*m/z*): 417 (M+Na). Purity 96.67% (UPLC/MS). HRMS *m/z*: [M+Na]: calcd. for $C_{23}H_{22}NaO_6$ 417.1314, found: 417.1302. FT-IR (ATR, υ) cm^{-1} 2915, 1849, 1730, 1597, 1511, 1468, 1309, 1250, 1173, 1098, 1025, 948, 823, 510. See Fig. S13 for RP-UPLC/MS chromatogram.

*4.1.4. General Procedure B (pentane-2,4-dione alkylation reaction, compounds **5** and **6**)*

A solution of pentane-2,4-dione (1.00 mmol) in dry THF (1.0 mL) was added to a stirred suspension of NaH (60% dispersion in mineral oil, 1.2 molar equiv) in dry THF (5.0 mL) at 0 °C and under N_2 atmosphere. The mixture was stirred at r.t. for 30 min, then the appropriate alkyl bromide (1.2 molar equiv) in THF (5.0 mL) was added dropwise at 0 °C and the resulting mixture was stirred overnight at r.t. Water (50 mL) was added at 0 °C, and the solution was extracted with Et_2O (3 × 50 mL); the combined organic layers were washed with brine, dried over Na_2SO_4, filtered, and the solvent was removed under reduced pressure. The obtained crude product was purified by FCC on silica gel using a mixture of PE/EtOAc as eluent.

*4.1.4.1. Ethyl (Z)-3-acetyl-4-hydroxypent-3-enoate (**5**-KE); ethyl 3-acetyl-4-oxopentanoate (**5**-KK).* Starting from pentane-2,4-dione (2.57 mL, 25.00 mmol) and ethyl 2-bromoacetate (3.33 mL, 30.00 mmol), a crude product was obtained. Purification by FCC (PE/EtOAc, 9.5:0.5) gave compound **5** as a colourless oil (1:2 mixture of KE/KK, 90% yield). ^{1}H NMR ($CDCl_3$): δ 1.20–1.28 (m, 6H, OCH_2CH_3, KE + KK), 2.13 (s, 6H, CH_3, KE), 2.24 (s, 6H, CH_3, KK), 2.85 (d, 2H, J = 7.2 Hz, CH_2COOCH$_2$CH$_3$, KK), 3.22 (s, 2H, CH_2COOCH$_2$CH$_3$, KE), 4.07–4.15 (m, 5H, OCH_2CH$_3$ KE + KK and CH KK). ^{13}C NMR ($CDCl_3$): δ 14.11 (OCH_2CH_3), 14.25 (OCH_2CH_3), 23.40 (CH_3), 26.29 (CH_3), 29.69 (2C, CH_3), 32.65 (CH_2COOCH$_2$CH$_3$), 33.36 (CH_2COOCH$_2$CH$_3$), 61.12 (2C, OCH_2CH$_3$), 61.24 (KK 3-CH), 104.44 (KE 3-C=), 171.29 (CO), 171.61 (CO), 191.96 (=COH), 202.65 (CO), 203.46 (2CO). FT-IR (ATR, n) cm-^{1} 2983, 2935, 1724, 1702, 1412, 1385, 1241, 1190, 1155, 1026, 951.

*4.1.4.2. tert-Butyl (Z)-3-acetyl-4-hydroxypent-3-enoate (**6**-KE) and tert-butyl 3-acetyl-4-oxopentanoate (**6**-KK).* Starting from pentane-2,4-dione (0.12 mL, 1.17 mmol) and tert-butyl-2-iodoacetate (0.40 g, 1.40 mmol), a crude product was obtained. Purification by FCC (PE/EtOAc, 9.5:0.5) gave compound **6** as a pale-yellow oil (1.1:1.0 mixture of KE/KK, 92% yield). ^{1}H NMR ($CDCl_3$): δ 1.43 (s, 18H, OC(CH_3)$_3$, KE + KK), 2.16 (s, 6H, CH_3, KE), 2.25 (s, 6H, CH_3, KK), 2.81 (d, 2H, J = 7.6 Hz, CH_2COOC(CH_3)$_3$, KK), 3.14 (s, 2H, CH_2COOC(CH_3)$_3$, KE), 4.07 (t, 1H, J = 7.6 Hz, CH, KK). ^{13}C NMR ($CDCl_3$): δ 28.09 (*t*-but CH_3), 28.15 (*t*-but CH_3), 29.45 (CH_3), 23.53 (CH_3), 23.35 (CH_3), 29.44 (CH_3), 34.54, (CH_2COO*t*-but), 33.94 (CH_2COO*t*-but), 63.66 (KK 3-CH), 81.29 (*t*-but Cq), 81.62 (*t*-but Cq), 104.81 (KE 3-C=), 202.70 (2C, CO), 191.55 (=COH), 170.75 (2C, CO). FT-IR (ATR, υ) cm^{-1} 2983, 2940, 1728, 1710, 1421, 1394, 1255, 1198, 1148, 1013, 966.

*4.1.5. (Z)-3-(1-hydroxyethylidene)hex-5-yn-2-one (**7**-KE) and 3-(prop-2-yn-1-yl)pentane-2,4-dione (**7**-KK)*

Propargyl bromide solution (16.86 mmol, 1.50 mL, 1.87 mL of 80 wt % in toluene) was added dropwise to a stirred suspension of pentane-2,4-dione (2.59 mL, 25.17 mmol), anhydrous K_2CO_3 (2.32 g, 16.86 mmol) and acetone (150 mL). The reaction mixture was heated at 80 °C for 6 h (monitored with TLC), hot filtered, and the filtrate was evaporated under reduced pressure. The obtained crude product was purified by FCC (PE/DCM 8:1), affording **7** as an off-white-pale yellow oil (1.7:1.0 KE/KK mixture, 60% yield). ^{1}H NMR ($CDCl_3$): δ 2.03 (t, 2H, J = 2.4 Hz, CH_2CCH, KE + KK), 2.18 (s, 6H, CH_3, KE), 2.26 (s, 6H, CH_3, KK), 2.70 (dd, 2H, J = 2.8 and 7.2 Hz, CH_2CCH, KK), 2.99 (d, 2H, J = 2.4 Hz, CH_2CCH, KE), 3.86 (t, 1H, J = 7.2 Hz, CH, KK). ^{13}C NMR ($CDCl_3$): δ 17.35 (2C, CH_2CCH); 23.11 (CH_3), 29.23 (CH_3), 66.64 (KK 3-CH), 68.71 (CH_2CCH), 70.43 (CH_2CCH), 80.43 (CH_2CCH), 81.62 (CH_2CCH), 106.43 (KE 3-C=), 190.92 (=COH), 202.17 (2C, CO). FT-IR (ATR, υ) cm^{-1} 3300, 3028, 1730, 1700, 1600, 1420, 1360, 1150, 645.

*4.1.6. General Procedure C (CuAAC, compounds **3** and **4**)*

To a stirred solution of **8** (1.00 mmol) and the appropriate azido derivative (1.3 molar equiv) in DMSO (4.35 mL), TEA (0.1 molar equiv) was added dropwise, followed by slow addition of a solution of $CuSO_4$ (0.1 molar equiv) and (+)-sodium L-ascorbate (0.5 molar equiv) in water (0.5 mL). The resulting mixture was diluted with DMSO (2.82 mL) and stirred overnight at r.t. Water was added, and the solution was extracted with DCM (3 × 25 mL). The combined organic phases were dried over Na_2SO_4, filtered, and evaporated under reduced pressure. The crude product was purified by FCC.

*4.1.6.1. Ethyl 2-(4-((2Z,4E)-3-hydroxy-5-(4-methoxyphenyl)-2-((E)-3-(4-methoxyphenyl)**acryloyl)penta-2,4-dien-1-yl)-1H-1,2,3-triazol-1-yl)acetate (3-KE) and ethyl 2-(4-((E)-5-(4-methoxyphenyl)-2-((E)-3-(4-methoxyphenyl)acryloyl)-3-oxopent-4-en-1-yl)-1H-1,2,3-triazol-1-yl)acetate (3-KK).* Alkyne intermediate **8** (0.30 g, 0.80 mmol) and azido intermediate **9** (0.13 g, 1.04 mmol) were reacted according to general procedure C. The crude product was purified by FCC (PE/EtOAc, 8.5:1.5) and crystallised from DCM/PE mixture to afford the desired compound **3** as an orange solid (1.5:1.0 mixture of KE/KK, 50% yield, mp 150–152 °C). ^{1}H NMR ($CDCl_3$): δ 1.18 (t, 3H, J = 7.2 Hz, OCH_2CH_3, KK), 1.26 (t, 3H, J = 7.2 Hz, OCH_2CH_3, KE), 3.44 (d, 2H, J = 7.2 Hz, CH_2, KK), 3.84 (s, 12H, OCH_3, KE + KK), 4.09 (s, 2H, CH_2, KE), 4.16 (q, 2H, J = 7.2 Hz, OCH_2CH$_3$, KK), 4.22 (q, 2H, J = 7.2 Hz, OCH_2CH$_3$, KE), 4.77 (t, 1H, J = 7.2 Hz, CH, KK), 5.08 (s, 4H, NCH_2, KE + KK), 6.74 (d, 2H, J = 16.0 Hz, CO-CHα=CHβ, KK), 6.90 (d, 8H, J = 8.4 Hz, Ar, KE + KK), 6.95 (d, 2H, J = 15.6 Hz, CO-CHα=CHβ, KE), 7.38 (s, 1H, KE), 7.50 (d, 4H, J = 8.4 Hz, Ar, KE), 7.51 (d, 4H, J = 8.0 Hz, Ar, KK), 7.55 (s, 1H, KK), 7.66 (d, 2H, J = 16.0 Hz, CO-CHα=CHβ, KK), 7.75 (d, 2H, J = 15.2 Hz,

CO-CHα=CHβ, KE). ^{13}C NMR ($CDCl_3$): δ 14.1 ($OCH_2\underline{CH_3}$), 14.2 ($OCH_2\underline{CH_3}$), 23.3 (CH_2), 24.8 (CH_2), 51.1 (2C, NCH_2), 55.5 (4C, OCH_3), 62.5 ($O\underline{CH_2}CH_3$), 62.6 ($O\underline{CH_2}CH_3$), 63.1 (KK 4-CH), 107.7 (KE 4-C=), 114.5 (8C, CH-Ar), 118.0 (2C, CO-CHα=CHβ), 122.2 (2C, CO-CHα=CHβ), 127.0 (2C, Cq-Ar), 128.1 (2C, Cq-Ar), 130.2 (4C, CH-Ar), 130.7 (4C, CH-Ar), 142.3 (2C, CO-CHα=CHβ), 145.00 (2C, CO-CHα=CHβ), 161.6 (2C, Cq-Ar), 162.2 (2C, Cq-Ar), 166.2 (2C, CO), 183.4 (2C, CO and =COH), 194.5 (2C, CO). See Fig. S9 for ^{1}H NMR and ^{13}C NMR spectra and Fig. S10 for 2D ^{1}H–^{1}H COSY and 2D ^{1}H–^{13}C HSQC spectra. Formula $C_{28}H_{29}N_3O_6$, MW: 503.55, ESI-MS (*m/z*): 526 (M+Na). Purity 95.17% (UPLC/MS). HRMS *m/z*: [M+Na]: calcd. for $C_{28}H_{29}N_3NaO_6$ 526.1949, found 526.1927. FT-IR (ATR, υ) cm^{-1} 1753, 1594, 1509, 1421, 1249, 1166, 1098, 1024, 969, 825, 517. See Fig. S13 for RP-UPLC/MS chromatogram.

*4.1.6.2. (1E,4Z,6E)-4-((1-butyl-1H-1,2,3-triazol-4-yl)methyl)-5-hydroxy-1,7-bis(4 methoxyphenyl) hepta-1,4,6-trien-3-one (**4**-KE).* Alkyne intermediate **8** (0.30 g, 0.80 mmol) and azido intermediate **10** (0.13 g, 1.04 mmol) were reacted according to general Pprocedure C. The crude product was purified by FCC (PE/EtOAc, 8.5:1.5) and crystallised from DCM/PE mixture to afford the desired compound **4** as an orange solid (46% yield), mp 121–122 °C. ^{1}H NMR ($CDCl_3$): δ 0.83 (t, 3H, *J* = 7.2 Hz, CH_3), 1.20–1.29 (m, 2H, CH_2), 1.76–1.84 (m, 2H, CH_2), 3.83 (s, 6H, OCH_3), 4.05 (s, 2H, CH_2), 4.25 (t, 2H, *J* = 7.2 Hz, NCH_2), 6.89 (d, *J* = 8.0 Hz, 4H, Ar), 6.92 (d, 2H, *J* = 16.0 Hz, CO-CHα=CHβ), 7.19 (s, 1H, CH-Ar), 7.47 (d, 4H, *J* = 8.3 Hz, Ar), 7.74 (d, 2H, *J* = 15.4 Hz, CO-CHα=CHβ). ^{13}C NMR ($CDCl_3$): δ 13.5 (CH_3), 19.8 (CH_2), 23.4 (CH_2), 32.3 (CH_2), 51.3 (NCH_2), 55.6 (2C, OCH_3), 108.0 (4-C=), 114.6 (4C, CH-Ar), 118.0 (2C, CO-CHα=CHβ), 121.8 (CH-Ar), 128.1 (2C, Cq-Ar), 130.2 (4C, CH-Ar), 142.1 (2C, CO-CHα=CHβ), 161.6 (2C, Cq-Ar), 183.4 (2C, CO and =COH). See Fig. S11 for ^{1}H NMR and ^{13}C NMR spectra and Fig. S12 for 2D ^{1}H–^{1}H COSY and 2D ^{1}H–^{13}C HSQC spectra. Formula $C_{28}H_{31}N_3O_4$, MW: 473.57, ESI-MS (*m/z*): 474 (M+H). HRMS *m/z*: [M+Na]: calcd. for $C_{28}H_{31}N_3NaO_4$ 496.2206; found 496.2187. FT-IR (ATR, υ) cm^{-1} 1600, 1508, 1421, 1243, 1170, 1027, 966, 822, 514. Purity 97.66% (UPLC/MS).). See Fig. S13 for RP-UPLC/MS chromatogram.

*4.1.7. General Procedure D (azido intermediates **9** and **10**)*

The appropriate alkyl halide (1.00 mmol) was slowly added to a solution of NaN_3 (5.0 molar equiv) in acetone/H_2O (4:1, 10.0 mL) and the resulting mixture was allowed to stir overnight at r.t. Water (10 mL) was added, and the solution was extracted with EtOAc (3 × 20 mL). The combined organic layers were washed with brine, dried over Na_2SO_4, filtered and concentrated under reduced pressure. The resulting crude was employed in the next synthetic step without purification.

*4.1.7.1. Ethyl azidoacetate (**9**).* Ethyl bromoacetate (1.10 mL, 10.00 mmol) and NaN_3 (3.25 g, 50.00 mmol) were allowed to react according to general procedure D to afford **6** as pale-yellow oil (43% yield).

*4.1.7.2. 1-azidobutane (**7**).* 1-Bromobutane (1.10 mL, 10.00 mmol) and NaN_3 (3.25 g, 50.00 mmol) were allowed to react according to general procedure D to afford **7** as pale-yellow oil (56% yield).

4.2. Biological studies

4.2.1. Reagents

Tissue culture media, antibiotics, and fetal bovine serum (FBS) were obtained from Thermo Fisher Scientific (Waltham, MA, USA). LPS (Ultra-Pure LPS-EB from Escherichia coli, 0111:B4 strain) was purchased from InvivoGen (InvivoGen Europe, Toulouse, France). Enzyme-linked immunosorbent assay (ELISA) kits were obtained from Antigenix America (Huntington Station, NY, USA). Falcon tissue culture plastic-wares were purchased from BD. Biosciences (SACCO srl, Cadorago (C. O.), Italy). All samples containing curcumin and derivatives were kept protected from light throughout all experiments.

Synthetic Aβ42 was purchased from AnaSpec (Fremont, CA, USA) as lyophilised powder and stored at −20 °C. 1,1,1,3,3,3-Hexafluoropropan-2-ol (HFIP), acetonitrile (ACN), sodium carbonate (Na_2CO_3) sodium phosphate (Na_2HPO_4 and NaH_2PO_4) were supplied by Sigma-Aldrich (St. Louis, MO). Ethanol 96° was supplied by Carlo Erba (Cornaredo, Italy). Sodium hydroxide (NaOH) was provided by Merck (Darmstadt, Germany).

4.2.2. Cell cultures

4.2.2.1. Primary microglia cell cultures. All experiments were performed in accordance with EU Directive (2010/63/EU) for the care and use of laboratory animals and those of the Italian Ministry of Health (DL 26/2014) and were approved by the Institutional Review Board for Animal Research of the University of Padua and by the Italian Ministry of Health (protocol number 41451.N.N8P).

Microglia were isolated from mixed glial cell cultures as previously described [66]. Briefly, cells were prepared from the cerebral cortices of postnatal day 1 Sprague-Dawley rat pups (CD strain), plated in 75 cm^2 poly-L-lysine-coated tissue culture flasks (1.5 brains per flask) and grown in high-glucose Dulbecco's modified Eagle's medium (DMEM) supplemented with 2 mM glutamine, 10% heat-inactivated FBS, 1% penicillin/streptomycin, and 50 μg/mL gentamycin (growth medium). Culture medium was changed after 24 h. Seven days after isolation, mixed glial cultures reached confluence and microglia were separated from the astroglial monolayer by shaking the flasks on an orbital shaker at 200 rpm for 1 h (37 °C), re-suspended in the growth medium, and plated on poly-L-lysine-coated plastic wells at a density of 1.50 × 10^5 cells/cm^2. Cells were allowed to adhere for 45 min and then washed to remove non-adhering cells. Cultures obtained using this procedure generated 97% microglia immunopositive to a primary polyclonal antibody against ionised calcium-binding adaptor molecule 1 (Iba1, 1:800, Wako Chemicals USA Inc., Richmond, VA, USA, Cat. 019–19741), a marker for microglia cell types [29]. Cells were maintained at 37 °C in a humidified atmosphere containing 5% CO_2. LPS was dissolved in endotoxin-free Water (InvivoGen). Curcumin and its derivatives were solubilised in dimethylsulfoxide (DMSO) and added to the cultures so as not to exceed 0.1% of the total volume. Control cultures contained the same concentration of DMSO.

4.2.2.2. Neuroblastoma cells. Human neuronal SH-SY5Y cells (Sigma-Aldrich, St. Louis, MO, USA) were routinely grown in DMEM supplemented with 10% FBS, 2 mM L-glutamine, 50 U/mL penicillin, and 50 μg/mL streptomycin at 37 °C in a humidified incubator with 5% CO_2.

4.2.3. MTT assay

4.2.3.1. Primary microglia cultures. Microglia viability was evaluated by a quantitative colourimetric method utilising the metabolic dye MTT [28,67]. Cells were seeded at the density of 6 × 10^4 cells/well in 96-well plates and incubated overnight at 37 °C in a 5% CO_2 atmosphere. Growth medium was replaced with serum-free medium 1 h before treatment for 24 h with increasing concentrations (1–20 μM) of compounds **1**, **2a-c**, **3**, and **4**. **Curc**, in the same concentration range, was used as a positive control. After treatment, the medium was removed, and the cells were incubated with MTT (0.18 mg/mL) in a humidified incubator at 37 °C for 4 h. Afterwards, the supernatants were removed, and the formazan crystals developed in the viable cells were solubilised with DMSO. The plates were then read on a microplate reader (Victor2 Multilabel Counter, Wallac, Cambridge, MA, USA) using a test wavelength of 570 nm and a reference wavelength of 630 nm. Absorbance of vehicle-treated cells was considered as 100% of cell viability.

4.2.3.2. Neuroblastoma cells. SH-SY5Y cells were seeded in a 96-well plate at 2×10^4 cells/well, incubated for 24 h and then treated with different concentrations (1.25–40 μM) of compounds **1**, **2a**, **3**, and **4** for 24 h at 37 °C in 5% CO_2. The cell viability, in terms of mitochondrial metabolic function, was evaluated by the reduction of MTT to its insoluble formazan. Briefly, the treatment was replaced with MTT in Hanks' Balanced Salt solution (HBSS, 0.5 mg/mL) for 2 h at 37 °C in 5% CO_2. After washing with HBSS, formazan crystals were dissolved in isopropanol. The amount of formazan was measured (570 nm, reference filter 690 nm) using a multilabel plate reader (VICTOR™ X3, PerkinElmer, Waltham, MA, USA).

4.2.4. Cytokine determination

Primary microglia were pretreated for 1 h with increasing non-cytotoxic concentrations of the compounds and then stimulated with 100 ng/mL of LPS for an additional 24 h. At the end of treatment, culture media were collected, and TNF-α and IL-1β assayed using commercially available ELISA kits, according to the manufacturer's instructions. Cytokine concentrations (pg/mL) in the medium were determined by reference to standard curves obtained with known amounts of TNF-α or IL-1β. The results were expressed as a percentage relative to LPS-stimulated cultures.

4.2.5. Determination of intracellular GSH formation

SH-SY5Y cells were seeded in a black 96-well plate at 2×10^4 cells/well, incubated for 24 h, and then treated with compounds **1**, **2a**, **3** and **4** at the concentration of 2.5 μM for 24 h at 37 °C in 5% CO_2. At the end of incubation, the treatment was replaced with the fluorescent probe H_2DCF-DA. After 30 min of incubation at 37 °C, glutathione levels were measured (excitation at 355 nm and emission at 460 nm) using a multilabel plate reader (VICTOR™ X3, PerkinElmer). Data are expressed as concentrations of GSH (μM) obtained by a GSH standard curve.

4.2.6. Determination of intracellular ROS formation

SH-SY5Y cells were seeded in a 96-well plate at 2×10^4 cells/well, incubated for 24 h (the time necessary to activate the endogenous antioxidant system), and then treated with compounds **1**, **2a**, **3** and **4** at the concentration of 2.5 μM for 24 h at 37 °C in 5% CO_2. At the end of incubation, the treatment was replaced with the fluorescent probe H_2DCF-DA. After 30 min of incubation at room temperature, the probe was removed, and cells were incubated with t-BuOOH (50 μM) for 30 min at room temperature. ROS levels were measured (excitation at 485 nm and emission at 535 nm) using a multilabel plate reader (VICTOR™ X3, PerkinElmer). Data are expressed as percentages of ROS increase.

4.2.7. Determination of Nrf2 nuclear translocation by western blotting

SH-SY5Y cells were seeded in 60 mm dishes at 2×10^6 cells/dish, incubated for 24 h, and then treated with compounds **1**, **2a**, **3** and **4** at the concentration of 2.5 μM for 3 h at 37 °C in 5% CO_2. At the end of treatment, cytosolic and nuclear extractions for Nrf2 nuclear translocation were performed by using a Nuclear Extract Kit (Active Motif, Carlsbad, CA, USA), according to the manufacturer's guidelines. Cytosolic and nuclear extracts (50 μg per sample) were separated by SDS-polyacrylamidegels and transferred onto nitrocellulose membranes, which were probed with primary Nrf2 (1:1000; Santa Cruz Biotechnology, Dallas, TX, USA) and secondary antibodies. ECL reagents (Thermo Scientific Pierce, Milano, Italy) were utilised to detect targeted bands. The same membranes were stripped and reprobed with β-actin antibody (1:1000; Sigma-Aldrich, St. Louis, MO, United States) and Laminin B1 (1:1000; Santa Cruz Biotechnology, Dallas, TX, USA). Data were normalised on the β-actin and Laminin B1 bands for cytosolic and nuclear extracts, respectively, and analysed by densitometry using the Quantity One software (Bio-Rad Laboratories Srl, Hercules, CA, USA). Data are expressed as a ratio between nuclear and cytoplasmatic Nrf2 levels.

4.2.8. Real-time polymerase chain reaction microglia cells

Microglia were pretreated for 1 h with the compounds and then stimulated with 100 ng/mL Ultra-Pure LPS-EB for an additional 6 h. At the end of incubation, total RNA was extracted from cells by QIAzol lysis reagent (Qiagen, Hilden, Germany), according to the manufacturer's instructions. RNA integrity and quantity were determined by RNA 6000 Nano assay in an Agilent BioAnalyser (Santa Clara, CA, USA). Reverse transcription was performed with SuperScript IV reverse transcriptase (Thermo Fisher Scientific, Milano, Italy). The real-time PCR reaction was performed as described previously [68]. Primer sequences were: β-actin, 5′-GATCAGCAAGCAGGAGTACGATGA-3′, 5′-GGTGTAAAACG-CAGCTCAGTAACA-3'; IL-1β, 5′-CGTCCTCTGTGACTCGTGGG-3′, 5′-ATGGGTCAGACAGCACGAGG-3'; NLRP3, 5′-TGATGCATGCACG TCTAATCTC-3′, 5′-CAAATCGAGATGCGGGAGAG-3'; TNF-α, 5′-GCAGGTTCCGTCCCTCTCAT-3′, 5′-TGCCAGTTCCACATCTCGGA-3'. Amounts of each gene product were calculated using linear regression analysis from standard curves, demonstrating amplification efficiencies ranging from 90 to 100%. Dissociation curves were generated for each primer pair, showing single-product amplification. Data are presented as specific ratio between the gene of interest and the reference gene β-actin.

4.2.9. Capillary electrophoresis

Aβ42 peptide was solubilised according to a protocol recently reported by us in Ref. [29]. Briefly, lyophilised Aβ42 was dissolved in HFIP (1 mg/mL, 221 μM) and kept at 4 °C for 30 min. The solution was then aliquoted in microfuge tubes and the solvent was evaporated by Eppendorf Concentrator plus® (Hamburg, Germany). The Aβ42 aliquots were redissolved in a basic mixture (ACN/300 μM Na_2CO_3/113 mM NaOH, 48.3:48.3:3.4 v/v/v) to obtain 500 μM Aβ42. This stock solution was then diluted to the operative concentration (221 μM Aβ42 control peptide) with 20 mM NaH_2PO_4/Na_2HPO_4 pH 7.4, with or without small molecules. Stock solutions of all compounds (1.53 mM) were prepared in pure ethanol.

For coincubation studies, Aβ42 stock solution in the basic mixture was diluted with a proper amount of phosphate buffer containing the compound, so to obtain the desired compound concentration. Aβ42 aggregation process in the absence/presence of curcumin analogues and curcumin was monitored by an Agilent Technologies 3D CE system with a built-in diode-array detector (Waldbronn, Germany). For the separation, a fused silica capillary (total length: 33 cm, 24.5 cm to the detector, Polymicro Technologies, Phoenix, AZ, USA) was employed. The background electrolyte (BGE) consisted of 80 mM NaH_2PO_4/Na_2HPO_4 at pH 7.4. BGE solutions were prepared daily using Millipore Direct-Q deionised water (Bedford, MA) and filtered on 0.45 μm Sartorius membrane filters (Göttingen, Germany). Samples were injected hydrodynamically, by applying a pressure of 30 mbar for 3 s at the anodic end of the capillary. Separation voltage was +12 kV (operative current: 80–85 μA). The capillary was thermostatted at 25 °C and the detection wavelength was set at 200 nm. The electrosmotic flow (EOF) was measured as a perturbation of the baseline given by the sample solvent mixture. Oligomeric species were identified on the basis of their effective mobility (μeff), which was calculated by subtracting the contribute of the EOF from the apparent mobility (μapp). Semiquantitative analyses of the separated oligomers were performed based on the normalised area % [50].

4.2.10. Fly strains and materials

Fly stocks were raised on standard medium (yeast 27 g/L, agar 10 g/L, corn meal 22 g/L, molasses 66 mL/L, nipagin 2.5 g/L, 12.5 mL/L ethanol 96%) and in standard conditions at 22 °C and 12:12 h light:dark cycle. The *Drosophila* strains Tubulin-Gal4 (BL-5138) and W1118 (BL-5905) were obtained from the Bloomington Drosophila Stock Center. The UAS-Dspastin-RNAi *Drosophila* line used in this study was described previously [69]. Gal4/UAS crossings were performed at 28 °C.

4.2.11. Eclosion rate

Female virgins and males were placed in a vial in a 10:5 ratio and allowed to lay eggs for 48 h. Then, adults were removed from the tubes and larvae were allowed to develop. Pupae and flies that eclosed were counted, and data expressed as percent of eclosion (number of adult flies eclosed/number of pupae). Six vials for each genotype were used [60].

4.2.12. Real-time PCR in Drosophila

The relative expression levels of Nrf2, SOD1 and CAT were determined using quantitative real-time PCR. Total RNA was isolated from 5 third instar larvae and was extracted and purified using Total RNA purification kit (Norgen Biotek Corp. Thorold, ON, CA) according to the manufacturer's instructions. The concentration and purity of RNA samples were determined using a NanoDrop 2000c Spectrophotometer (Thermo Fisher Scientific). Real-time PCR (qPCR) was performed on Eco Real-Time PCR System (Illumina Inc. San Diego, CA, USA), using One-Step SYBR® Prime Script TM RT-PCR Kit II (Takara-Clontech, Kusatsu, Japan) as in Ref. [70]. The housekeeping Rp49 gene was used as an internal control to normalise the data. Relative mRNA expression levels were calculated by the threshold cycle (Ct) value of each PCR product and normalised using a comparative 2–ΔΔCt method. Data represented are the result of five independent biological replicates. Each biological sample was loaded in triplicate. Tubulin-Gal4/+ *Drosophila* line was used as control [71]. Primers used were: Nrf2 F: 5′-GAGGTGGAAATCGGAGATGA-3′ and R: 5′-CTGCTTGTAGAGCACCTCAGC-3'; CAT F: 5′- ATGCGGCTTCCAATCAGTTG-3′ and R: 5′-GGTGGTAATGGCACCAGGAG-3'; SOD1 F: 5′- ATTAACGGCGAT GCCAAGGG-3′ and R: 3′-CCATTGGTGTTGTCACCGAAC-3'; Rp49 F: 5′-AGGCCCAAGATCGTGAAGAA-3′ and R: 5′-TCGATACCCTTGGGC TTGC-3'.

4.2.13. Oxidative stress detection in Drosophila and imaging acquisition

Dihydroethidium (DHE, Sigma Aldrich) was used to detect ROS levels in *Drosophila* larvae. DHE is a cell-permeant reagent that is oxidised by intracellular ROS and forms red fluorescent species. DHE is oxidised by superoxide anion to form 2-hydroxyethidium (2-OH-E^+, ex 500–530 nm/em 590–620 nm) or by non-specific oxidants to generate ethidium (E^+, ex 480 nm/em 576 nm) [72].

For the analysis of the effects of **3** and **4** *in vivo*, larvae raised in drug enriched food at 28 °C were harvested and dissected in HL3. Then, whole larvae were stained with DHE at 30 μM in HL3 for 30 min and fixed in 4% PFA for 10 min. Following fixation, larvae were washed in PBS containing 0.3% Triton X-100 and stained with DAPI (Invitrogen, Thermo Fisher Scientific) for 30 min, washed and mounted on glass slides using Mowiol 4–88 (Merck Life Science) [73].

Muscle and brain images of fixed larvae were acquired using a confocal microscope ZEISS LSM 800 Confocal Laser Scanning Microscope (Carl Zeiss Microscopy, Oberkochen, Germany), equipped with a Zeiss 63x/1.4– Plan-Apochromat oil objective, by using the ZEN Blue acquisition software. To discriminate 2-OH-E^+ from E^+ the DHE signal was captured between 580 nm and 630 nm.

For the quantification of DHE and DAPI intensity, ImageJ was used to produce maximum intensity projections of the Z-stacks. The red channel of DHE and the blue channel of DAPI were analysed separately for each image. Channels were converted to 8-bit images and the measure tool was used to quantify the mean intensity of the DHE and DAPI signal. For each sample, two muscles were acquired and two Region of Interest (ROI) of 2500 μm^2 per muscle were analysed. For each brain, two ROI of 1900 μm^2 were analysed. For each group, ten to fifteen larvae were used. Fluorescence values are expressed as the relative intensity of DHE with respect to DAPI intensity (DHE/DAPI fluorescence ratio).

4.2.14. Statistics

Data were analysed using GraphPad Prism Software, version 8.0 (GraphPad Software, Inc., San Diego, CA, USA). A value of $p < 0.05$ was considered to indicate statistically significant differences.

4.3. Computational methods

Ten NMR structures of β-amyloid fibril (PDB Id: 2MXU) [74] were used for the computational study. The structures of the fibril were protonated according to physiological pH, and the ligands were prepared as described in the previous work [27]. Ensemble blind docking of the ligands (i.e., **curc**, compounds **1**, **2a**, **3**, **4**) was performed on each of the NMR β-amyloid structures, using PLANTS [75] the ChemPLP scoring function, speed1 as accuracy level and generating 100 poses per ligand, obtaining 1000 poses per ligands overall.

These poses were clustered according to ligands RMSDs, using CPPTRAJ [76] and a hierarchical algorithm [77], as reported in previous studies [78]. The clusterisation led to the identification of six main binding hot-spots. For each cluster belonging to a specific spot (C_i), we computed the average docking score (C_is), which was weighted on the cluster population (C_ip). As a result, each spot was associated to a score for the different ligands (i.*e.,* $\frac{(C_1 s \cdot C_1 p)+(C_2 s \cdot C_2 p)+\ldots+(C_n s \cdot C_n p)}{C_1 p+C_2 p+\ldots+C_n p}$ [76].

Author contributions

Conceptualisation, F.B, E.D.L., M.Z.; methodology, F.B, E.D.L., M.Z., A.T., G.V., G.O.; formal analysis, C.C., R.M.C.D.M., F.S., S.Ge, G.Gu., L. P., C.A., G.Gh.; data curation, M.S., A.B., S.Go.; writing and original draft preparation, C.C., R.M.C.D.M., F.S., S.Ge, G.G., L.P; writing and review and editing, F.B, E.D.L., M.Z.; supervision, F.B, E.D.L., M.Z.; funding acquisition, F.B, E.D.L., M.Z.; All authors have read and agreed to the published version of the manuscript.

Funding sources

R.M.C.D.M and F.S. acknowledge a PostDoc scholarship from the Department of Pharmacy and Biotechnology, University of Bologna. This work was supported by project PRIN 2017 (2017MT3993_007), funded by the Italian Ministry of University and Research (MIUR) and from PROGETTO DI ATENEO, funded by University of Padua, Italy (ZUSS_SID18_01).

Declaration of competing interest

The authors declare the following financial interests/personal relationships which may be considered as potential competing interests: Alessandra Bisi and Morena Zusso reports financial support was provided by Italian Ministry of University and Research (MIUR).

Data availability

Data will be made available on request.

Appendix A. Supplementary data

Supplementary data to this article can be found online at.

Appendix B. Supplementary data

Supplementary data to this article can be found online at https://doi.org/10.1016/j.ejmech.2023.115297.

References

[1] Alzheimer's disease facts and figures, Alzheimers Dis. Dement. (n.d.). https://www.alz.org/alzheimers-dementia/facts-figures (accessed December 19, 2022).
[2] J.A. Hardy, G.A. Higgins, Alzheimer's disease: the amyloid cascade hypothesis, Science 256 (1992) 184–185, https://doi.org/10.1126/science.1566067.
[3] S. Li, D.J. Selkoe, A mechanistic hypothesis for the impairment of synaptic plasticity by soluble Aβ oligomers from Alzheimer's brain, J. Neurochem. 154 (2020) 583–597, https://doi.org/10.1111/jnc.15007.

[4] D.M. Walsh, D.J. Selkoe, Amyloid β-protein and beyond: the path forward in Alzheimer's disease, Curr. Opin. Neurobiol. 61 (2020) 116–124, https://doi.org/10.1016/j.conb.2020.02.003.

[5] T. Yang, S. Li, H. Xu, D.M. Walsh, D.J. Selkoe, Large soluble oligomers of amyloid β-protein from alzheimer brain are far less neuroactive than the smaller oligomers to which they dissociate, J. Neurosci. 37 (2017) 152–163, https://doi.org/10.1523/JNEUROSCI.1698-16.2016.

[6] A.J. Doig, Positive feedback loops in alzheimer's disease: the alzheimer's feedback hypothesis, J. Alzheimers Dis. 66 (2018) 25–36, https://doi.org/10.3233/JAD-180583.

[7] C. Domingues, O.A.B. da Cruz E Silva, A.G. Henriques, Impact of cytokines and chemokines on alzheimer's disease neuropathological hallmarks, Curr. Alzheimer Res. 14 (2017) 870–882, https://doi.org/10.2174/1567205014666170317113606.

[8] Z.-Z. Si, C.-J. Zou, X. Mei, X.-F. Li, H. Luo, Y. Shen, J. Hu, X.-X. Li, L. Wu, Y. Liu, Targeting neuroinflammation in Alzheimer's disease: from mechanisms to clinical applications, Neural Regen, Res. 18 (2023) 708, https://doi.org/10.4103/1673-5374.353484.

[9] S. Saha, B. Buttari, E. Profumo, P. Tucci, L. Saso, A perspective on Nrf2 signaling pathway for neuroinflammation: a potential therapeutic target in alzheimer's and Parkinson's diseases, Front. Cell. Neurosci. 15 (2022) 787258, https://doi.org/10.3389/fncel.2021.787258.

[10] S.M.U. Ahmed, L. Luo, A. Namani, X.J. Wang, X. Tang, Nrf2 signaling pathway: pivotal roles in inflammation, Biochim. Biophys. Acta, Mol. Basis Dis. 1863 (2017) 585–597, https://doi.org/10.1016/j.bbadis.2016.11.005.

[11] S. Saha, B. Buttari, E. Panieri, E. Profumo, L. Saso, An overview of Nrf2 signaling pathway and its role in inflammation, Molecules 25 (2020) 5474, https://doi.org/10.3390/molecules25225474.

[12] P. Youssef, B. Chami, J. Lim, T. Middleton, G.T. Sutherland, P.K. Witting, Evidence supporting oxidative stress in a moderately affected area of the brain in Alzheimer's disease, Sci. Rep. 8 (2018), 11553, https://doi.org/10.1038/s41598-018-29770-3.

[13] C. Lennicke, H.M. Cochemé, Redox signalling and ageing: insights from Drosophila, Biochem. Soc. Trans. 48 (2020) 367–377, https://doi.org/10.1042/BST20190052.

[14] S. Malacrida, F. De Lazzari, S. Mrakic-Sposta, A. Vezzoli, M.A. Zordan, M. Bisaglia, G.M. Menti, N. Meda, G. Frighetto, G. Bosco, T. Dal Cappello, G. Strapazzon, C. Reggiani, M. Gussoni, A. Megighian, Lifespan and ROS levels in different Drosophila melanogaster strains after 24 h hypoxia exposure, Biol. Open. 11 (2022), bio059386, https://doi.org/10.1242/bio.059386.

[15] Z. Sang, K. Wang, J. Dong, L. Tang, Alzheimer's disease: updated multi-targets therapeutics are in clinical and in progress, Eur. J. Med. Chem. 238 (2022), 114464, https://doi.org/10.1016/j.ejmech.2022.114464.

[16] R. Fu, Y. Sun, W. Sheng, D. Liao, Designing multi-targeted agents: an emerging anticancer drug discovery paradigm, Eur. J. Med. Chem. 136 (2017) 195–211, https://doi.org/10.1016/j.ejmech.2017.05.016.

[17] R. Morphy, C. Kay, Z. Rankovic, From magic bullets to designed multiple ligands, Drug Discov. Today 9 (2004) 641–651, https://doi.org/10.1016/S1359-6446(04)03163-0.

[18] A.G. Atanasov, S.B. Zotchev, V.M. Dirsch, C.T. Supuran, Natural products in drug discovery: advances and opportunities, Nat. Rev. Drug Discov. 20 (2021) 200–216, https://doi.org/10.1038/s41573-020-00114-z.

[19] J. Sharifi-Rad, Y.E. Rayess, A.A. Rizk, C. Sadaka, R. Zgheib, W. Zam, S. Sestito, S. Rapposelli, K. Neffe-Skocińska, D. Zielińska, B. Salehi, W.N. Setzer, N.S. Dosoky, Y. Taheri, M. El Beyrouthy, M. Martorell, E.A. Ostrander, H.A.R. Suleria, W.C. Cho, A. Maroyi, N. Martins, Turmeric and its major compound curcumin on Health: bioactive effects and safety profiles for food, pharmaceutical, biotechnological and medicinal applications, Front. Pharmacol. 11 (2020), 01021, https://doi.org/10.3389/fphar.2020.01021.

[20] I. Doytchinova, M. Atanasova, E. Salamanova, S. Ivanov, I. Dimitrov, Curcumin inhibits the primary nucleation of amyloid-beta peptide: a molecular dynamics study, Biomolecules 10 (2020) 1323, https://doi.org/10.3390/biom10091323.

[21] K.M. Nelson, J.L. Dahlin, J. Bisson, J. Graham, G.F. Pauli, M.A. Walters, The essential medicinal chemistry of curcumin, J. Med. Chem. 60 (2017) 1620–1637, https://doi.org/10.1021/acs.jmedchem.6b00975.

[22] A realistic view on "the essential medicinal chemistry of curcumin, ACS Med. Chem. Lett. 8 (2017) 893–896, https://doi.org/10.1021/acsmedchemlett.7b00284.

[23] S. Jasial, Y. Hu, J. Bajorath, How frequently are pan-assay interference compounds active? Large-scale analysis of screening data reveals diverse activity profiles, low global hit frequency, and many consistently inactive compounds, J. Med. Chem. 60 (2017) 3879–3886, https://doi.org/10.1021/acs.jmedchem.7b00154.

[24] J. Bajorath, Activity artifacts in drug discovery and different facets of compound promiscuity, F1000Research 3 (2014) 233, https://doi.org/10.12688/f1000research.5426.1.

[25] R.M.C. Di Martino, A. De Simone, V. Andrisano, P. Bisignano, A. Bisi, S. Gobbi, A. Rampa, R. Fato, C. Bergamini, D.I. Perez, A. Martinez, G. Bottegoni, A. Cavalli, F. Belluti, Versatility of the curcumin scaffold: discovery of potent and balanced dual BACE-1 and GSK-3β inhibitors, J. Med. Chem. 59 (2016) 531–544, https://doi.org/10.1021/acs.jmedchem.5b00894.

[26] R.M.C. Di Martino, L. Pruccoli, A. Bisi, S. Gobbi, A. Rampa, A. Martinez, C. Pérez, L. Martinez-Gonzalez, M. Paglione, E. Di Schiavi, F. Seghetti, A. Tarozzi, F. Belluti, Novel curcumin-diethyl fumarate hybrid as a dualistic GSK-3β inhibitor/nrf2 inducer for the treatment of Parkinson's disease, ACS Chem. Neurosci. 11 (2020) 2728–2740, https://doi.org/10.1021/acschemneuro.0c00363.

[27] F. Bisceglia, F. Seghetti, M. Serra, M. Zusso, S. Gervasoni, L. Verga, G. Vistoli, C. Lanni, M. Catanzaro, E. De Lorenzi, F. Belluti, Prenylated curcumin analogues as multipotent tools to tackle alzheimer's disease, ACS Chem. Neurosci. 10 (2019) 1420–1433, https://doi.org/10.1021/acschemneuro.8b00463.

[28] M. Zusso, G. Mercanti, F. Belluti, R.M.C. Di Martino, A. Pagetta, C. Marinelli, P. Brun, E. Ragazzi, R. Lo, S. Stifani, P. Giusti, S. Moro, Phenolic 1,3-diketones attenuate lipopolysaccharide-induced inflammatory response by an alternative magnesium-mediated mechanism, Br. J. Pharmacol. 174 (2017) 1090–1103, https://doi.org/10.1111/bph.13746.

[29] E. De Lorenzi, D. Franceschini, C. Contardi, R.M.C. Di Martino, F. Seghetti, M. Serra, F. Bisceglia, A. Pagetta, M. Zusso, F. Belluti, Modulation of amyloid β-induced microglia activation and neuronal cell death by curcumin and analogues, Int. J. Mol. Sci. 23 (2022) 4381, https://doi.org/10.3390/ijms23084381.

[30] E. Chainoglou, D. Hadjipavlou-Litina, Curcumin in Health and diseases: alzheimer's disease and curcumin analogues, derivatives, and hybrids, Int. J. Mol. Sci. 21 (2020), https://doi.org/10.3390/ijms21061975, 1975.

[31] R.M.C. Di Martino, A. Bisi, A. Rampa, S. Gobbi, F. Belluti, Recent progress on curcumin-based therapeutics: a patent review (2012-2016). Part II: curcumin derivatives in cancer and neurodegeneration, Expert Opin. Ther. Pat. 27 (2017) 953–965, https://doi.org/10.1080/13543776.2017.1339793.

[32] K. Przygońska, M. Pacewicz, W. Sadowska, J. Poznański, W. Bal, M. Dadlez, His6, His13, and His14 residues in Aβ 1–40 peptide significantly and specifically affect oligomeric equilibria, Sci. Rep. 9 (2019) 9449, https://doi.org/10.1038/s41598-019-45988-1.

[33] K. Brännström, T. Islam, L. Sandblad, A. Olofsson, A. The role of histidines in amyloid β fibril assembly. FEBS Lett, 591 (2017), 1167-1175. doi: 10.1002/1873-3468.12616.

[34] A. Rammohan, B.C. Venkatesh, N.M. Basha, G.V. Zyryanov, M. Nageswararao, Comprehensive review on natural pharmacophore tethered 1,2,3-triazoles as active pharmaceuticals, Chem. Biol. Drug Des. (2022) 1–23, https://doi.org/10.1111/cbdd.14148, 00.

[35] H.C. Kolb, M.G. Finn, K.B. Sharpless, Click chemistry: diverse chemical function from a few good reactions, Angew. Chem. Int. Ed. 40 (2001) 2004–2021, https://doi.org/10.1002/1521-3773(20010601)40:11<2004::AID-ANIE2004>3.0.CO;2-5.

[36] R.M.C. Di Martino, NATURALLY INSPIRED PRIVILEGED STRUCTURES IN DRUG DISCOVERY: MULTIFUNCTIONAL COMPOUNDS FOR ALZHEIMER'S DISEASE TREATMENT, PhD Thesis, Alma Mater Studiorum, University of Bologna, (n.d).

[37] F. Seghetti, R.M.C. Di Martino, E. Catanzaro, A. Bisi, S. Gobbi, A. Rampa, B. Canonico, M. Montanari, D.V. Krysko, S. Papa, C. Fimognari, F. Belluti, Curcumin-1,2,3-Triazole conjugation for targeting the cancer apoptosis machinery, Molecules 25 (2020) 3066, https://doi.org/10.3390/molecules25133066.

[38] H.J.J. Pabon, A synthesis of curcumin and related compounds, Recl. Trav. Chim. Pays-Bas. 83 (1964) 379–386, https://doi.org/10.1002/recl.19640830407.

[39] E. Ferrari, F. Pignedoli, C. Imbriano, G. Marverti, V. Basile, E. Venturi, M. Saladini, Newly synthesized curcumin derivatives: crosstalk between chemico-physical properties and biological activity, J. Med. Chem. 54 (2011) 8066–8077, https://doi.org/10.1021/jm200872q.

[40] N. Gresa-Arribas, C. Viéitez, G. Dentesano, J. Serratosa, J. Saura, C. Solà, Modelling neuroinflammation in vitro: a tool to test the potential neuroprotective effect of anti-inflammatory agents, PLoS One 7 (2012), e45227, https://doi.org/10.1371/journal.pone.0045227.

[41] G. Mercanti, E. Ragazzi, G. Toffano, P. Giusti, M. Zusso, Phosphatidylserine and curcumin act synergistically to down-regulate release of interleukin-1β from lipopolysaccharide-stimulated cortical primary microglial cells, CNS neurol. Disord. - Drug Targets. 13 (n.d.) 792–800, doi: 10.2174/1871527313666140414121723.

[42] S. Lively, L.C. Schlichter, Microglia responses to pro-inflammatory stimuli (LPS, IFNγ+TNFα) and reprogramming by resolving cytokines (IL-4, IL-10), Front. Cell. Neurosci. 12 (2018) 215, https://doi.org/10.3389/fncel.2018.00215.

[43] C. Cunningham, Microglia and neurodegeneration: the role of systemic inflammation, Glia 61 (2013) 71–90, https://doi.org/10.1002/glia.22350.

[44] B. Becher, S. Spath, J. Goverman, Cytokine networks in neuroinflammation, Nat. Rev. Immunol. 17 (2017) 49–59, https://doi.org/10.1038/nri.2016.123.

[45] A. Piovan, J. Battaglia, R. Filippini, V.D. Costa, L. Facci, C. Argentini, A. Pagetta, P. Giusti, M. Zusso, Pre- and early post-treatment with arthrospira platensis (spirulina) extract impedes lipopolysaccharide-triggered neuroinflammation in microglia, Front. Pharmacol. 12 (2021), https://doi.org/10.3389/fphar.2021.724993.

[46] K.L. Hanslik, T.K. Ulland, The role of microglia and the Nlrp3 inflammasome in alzheimer's disease, Front. Neurol. 11 (2020), 570711, https://doi.org/10.3389/fneur.2020.570711.

[47] S. Macedo Vaz, M. de Freitas Silva, G. dos Reis Rosa Franco, M. Jorge R. Guimarães, F. Motta R. da Silva, N. Gonçalves Castro, I. Alvim Guedes, L. E. Dardenne, M. Amaral Alves, R. Garrett da Costa, G. Beserra Pinheiro, L. Germino Veras, M. Renata Mortari, L. Pruccoli, A. Tarozzi, C. Viegas, Synthesis and biological evaluation of 4-hydroxy-methylpiperidinyl-N-benzyl-acylarylhydrazone hybrids designed as novel multifunctional drug candidates for Alzheimer's disease, Bioorg. Med. Chem. 71 (2022), 116952, https://doi.org/10.1016/j.bmc.2022.116952.

[48] K.S.T. Dias, C.T. de Paula, T. Dos Santos, I.N.O. Souza, M.S. Boni, M.J. R. Guimarães, F.M.R. da Silva, N.G. Castro, G.A. Neves, C.C. Veloso, M.M. Coelho, I.S.F. de Melo, F.C.V. Giusti, A. Giusti-Paiva, M.L. da Silva, L.E. Dardenne, I. A. Guedes, L. Pruccoli, F. Morroni, A. Tarozzi, C. Viegas, Design, synthesis and evaluation of novel feruloyl-donepezil hybrids as potential multitarget drugs for the treatment of Alzheimer's disease, Eur. J. Med. Chem. 130 (2017) 440–457, https://doi.org/10.1016/j.ejmech.2017.02.043.

[49] S. Sabella, M. Quaglia, C. Lanni, M. Racchi, S. Govoni, G. Caccialanza, A. Calligaro, V. Bellotti, E. De Lorenzi, Capillary electrophoresis studies on the aggregation process of β-amyloid 1-42 and 1-40 peptides, Electrophoresis 25 (2004) 3186–3194, https://doi.org/10.1002/elps.200406062.
[50] F. Bisceglia, A. Natalello, M.M. Serafini, R. Colombo, L. Verga, C. Lanni, E. De Lorenzi, An integrated strategy to correlate aggregation state, structure and toxicity of Aß 1-42 oligomers, Talanta 188 (2018) 17–26, https://doi.org/10.1016/j.talanta.2018.05.062.
[51] Y.-R. Huang, R.-T. Liu, The toxicity and polymorphism of β-amyloid oligomers, Int. J. Mol. Sci. 21 (2020) 4477, https://doi.org/10.3390/ijms21124477.
[52] D. Shea, C.-C. Hsu, T.M. Bi, N. Paranjapye, M.C. Childers, J. Cochran, C. P. Tomberlin, L. Wang, D. Paris, J. Zonderman, G. Varani, C.D. Link, M. Mullan, V. Daggett, α-Sheet secondary structure in amyloid β-peptide drives aggregation and toxicity in Alzheimer's disease, Proc. Natl. Acad. Sci. USA 116 (2019) 8895–8900, https://doi.org/10.1073/pnas.1820585116.
[53] R. Colombo, A. Carotti, M. Catto, M. Racchi, C. Lanni, L. Verga, G. Caccialanza, E. De Lorenzi, CE can identify small molecules that selectively target soluble oligomers of amyloid beta protein and display antifibrillogenic activity, Electrophoresis 30 (2009) 1418–1429, https://doi.org/10.1002/elps.200800377.
[54] S. Butini, M. Brindisi, S. Brogi, S. Maramai, E. Guarino, A. Panico, A. Saxena, V. Chauhan, R. Colombo, L. Verga, E. De Lorenzi, M. Bartolini, V. Andrisano, E. Novellino, G. Campiani, S. Gemma, Multifunctional cholinesterase and amyloid Beta fibrillization modulators. Synthesis and biological investigation, ACS Med. Chem. Lett. 4 (2013) 1178–1182, https://doi.org/10.1021/ml4002908.
[55] S. Brogi, S. Butini, S. Maramai, R. Colombo, L. Verga, C. Lanni, E. De Lorenzi, S. Lamponi, M. Andreassi, M. Bartolini, V. Andrisano, E. Novellino, G. Campiani, M. Brindisi, S. Gemma, Disease-modifying anti-alzheimer's drugs: inhibitors of human cholinesterases interfering with β-amyloid aggregation, CNS Neurosci. Ther. 20 (2014) 624–632, https://doi.org/10.1111/cns.12290.
[56] E. De Lorenzi, M. Chiari, R. Colombo, M. Cretich, L. Sola, R. Vanna, P. Gagni, F. Bisceglia, C. Morasso, J.S. Lin, M. Lee, P.L. McGeer, A.E. Barron, Evidence that the Human Innate Immune Peptide LL-37 may be a Binding Partner of Amyloid-β and Inhibitor of Fibril Assembly, J. Alzheimers Dis. 59 (2017) 1213–1226, https://doi.org/10.3233/JAD-170223.
[57] P.H.M. Torres, A.C.R. Sodero, P. Jofily, F.P. Silva-Jr, Key Topics in Molecular Docking for Drug Design. Int. J. Mol. Sci. 20 (2019) 4574, doi: doi.org/10.3390/ijms20184574..
[58] X. Zhang, Y. Tian, Z. Li, X. Tian, H. Sun, H. Liu, A. Moore, C. Ran, Design and synthesis of curcumin analogues for in vivo fluorescence imaging and inhibiting copper-induced cross-linking of amyloid beta species in alzheimer's disease, J. Am. Chem. Soc. 135 (2013) 16397–16409, https://doi.org/10.1021/ja405239v.
[59] M. Necula, R. Kayed, S. Milton, C.G. Glabe, Small molecule inhibitors of aggregation indicate that amyloid β oligomerization and fibrillization pathways are independent and distinct, J. Biol. Chem. 282 (2007) 10311–10324, https://doi.org/10.1074/jbc.M608207200.
[60] C. Vantaggiato, G. Orso, G. Guarato, F. Brivio, B. Napoli, E. Panzeri, S. Masotti, F. Maria Santorelli, M. Lamprou, S. Gumeni, E. Clementi, M. Teresa Bassi, Rescue of lysosomal function as therapeutic strategy for SPG15 hereditary spastic, paraplegia 146 (2023) 1103–1120, https://doi.org/10.1093/brain/awac308.
[61] C. Julien, A. Lissouba, S. Madabattula, Y. Fardghassemi, C. Rosenfelt, A. Androschuk, J. Strautman, C. Wong, A. Bysice, J. O'sullivan, G.A. Rouleau, P. Drapeau, J.A. Parker, F.V. Bolduc, Conserved pharmacological rescue of hereditary spastic paraplegia-related phenotypes across model organisms, Hum. Mol. Genet. 25 (2016) 1088–1099, https://doi.org/10.1093/hmg/ddv632.
[62] G. Wali, E. Liyanage, N.F. Blair, R. Sutharsan, J.-S. Park, A. Mackay-Sim, C.M. Sue, Oxidative stress-induced axon fragmentation is a consequence of reduced axonal transport in hereditary spastic paraplegia SPAST patient neurons, Front. Neurosci. 14 (2020) 401, https://doi.org/10.3389/fnins.2020.00401.
[63] S. Gumeni, C. Vantaggiato, M. Montopoli, G. Orso, Hereditary spastic paraplegia and future therapeutic directions: beneficial effects of small compounds acting on cellular stress, Front. Neurosci. 15 (2021), 660714, https://doi.org/10.3389/fnins.2021.660714.
[64] E. Owusu-Ansah, A. Yavari, U. Banerjee, A protocol for in vivo detection of reactive oxygen species, Protoc. Exch. (2008), https://doi.org/10.1038/nprot.2008.23.
[65] D. Yanagisawa, T. Kato, H. Taguchi, N. Shirai, K. Hirao, T. Sogabe, T. Tomiyama, K. Gamo, Y. Hirahara, M. Kitada, I. Tooyama, Keto form of curcumin derivatives strongly binds to Aβ oligomers but not fibrils, Biomaterials 270 (2021), 120686, https://doi.org/10.1016/j.biomaterials.2021.120686.
[66] L. Facci, M. Barbierato, M. Zusso, S.D. Skaper, P. Giusti, Serum amyloid A primes microglia for ATP-dependent interleukin-1β release, J. Neuroinflammation 15 (2018) 164, https://doi.org/10.1186/s12974-018-1205-6.
[67] T. Mosmann, Rapid colorimetric assay for cellular growth and survival: application to proliferation and cytotoxicity assays, J. Immunol. Methods 65 (1983) 55–63, https://doi.org/10.1016/0022-1759(83)90303-4.
[68] M. Barbierato, M. Borri, L. Facci, M. Zusso, S.D. Skaper, P. Giusti, Expression and differential responsiveness of central nervous system glial cell populations to the acute phase protein serum amyloid A, Sci. Rep. 7 (2017), 12158, https://doi.org/10.1038/s41598-017-12529-7.
[69] N. Trotta, G. Orso, M.G. Rossetto, A. Daga, K. Broadie, The hereditary spastic paraplegia gene, spastin, regulates microtubule stability to modulate synaptic structure and function, Curr. Biol. CB. 14 (2004) 1135–1147, https://doi.org/10.1016/j.cub.2004.06.058.
[70] C. De Filippis, B. Napoli, L. Rigon, G. Guarato, R. Bauer, R. Tomanin, G. Orso, Drosophila D-idua reduction mimics mucopolysaccharidosis type I disease-related phenotypes, Cells 11 (2021) 129, https://doi.org/10.3390/cells11010129.
[71] B. Napoli, S. Gumeni, A. Forgiarini, M. Fantin, C. De Filippis, E. Panzeri, C. Vantaggiato, G. Orso, Naringenin ameliorates Drosophila ReepA hereditary spastic paraplegia-linked phenotypes, Front. Neurosci. 13 (2019) 1202, https://doi.org/10.3389/fnins.2019.01202.
[72] Y. Zhang, M. Dai, Z. Yuan, Methods for the detection of reactive oxygen species, Anal. Methods 10 (2018) 4625–4638, https://doi.org/10.1039/C8AY01339J.
[73] A. Forgiarini, Z. Wang, C. D'Amore, M. Jay-Smith, F.F. Li, B. Hopkins, M. A. Brimble, A. Pagetta, S. Bersani, S.D. Martin, B. Napoli, S. Bova, D. Rennison, G. Orso, Live applications of norbormide-based fluorescent probes in Drosophila melanogaster, PLoS One 14 (2019), e0211169, https://doi.org/10.1371/journal.pone.0211169.
[74] Y. Xiao, B. Ma, D. McElheny, S. Parthasarathy, F. Long, M. Hoshi, R. Nussinov, Y. Ishii, Aβ(1–42) fibril structure illuminates self-recognition and replication of amyloid in Alzheimer's disease, Nat. Struct. Mol. Biol. 22 (2015) 499–505, https://doi.org/10.1038/nsmb.2991.
[75] O. Korb, T. Stützle, T.E. Exner, PLANTS: application of ant colony optimization to structure-based drug design, in: M. Dorigo, L.M. Gambardella, M. Birattari, A. Martinoli, R. Poli, T. Stützle (Eds.), Ant Colony Optim. Swarm Intell., Springer, Berlin, Heidelberg, 2006, pp. 247–258, https://doi.org/10.1007/11839088_22.
[76] D.R. Roe, T.E. Cheatham, PTRAJ and CPPTRAJ: software for processing and analysis of molecular dynamics trajectory data, J. Chem. Theor. Comput. 9 (2013) 3084–3095, https://doi.org/10.1021/ct400341p.
[77] J. Shao, S.W. Tanner, N. Thompson, T.E. Cheatham, Clustering molecular dynamics trajectories: 1. Characterizing the performance of different clustering algorithms, J. Chem. Theor. Comput. 3 (2007) 2312–2334, https://doi.org/10.1021/ct700119m.
[78] S. Gervasoni, G. Malloci, A. Bosin, A.V. Vargiu, H.I. Zgurskaya, P. Ruggerone, Recognition of quinolone antibiotics by the multidrug efflux transporter MexB of Pseudomonas aeruginosa, Phys. Chem. Chem. Phys. 24 (2022) 16566–16575, https://doi.org/10.1039/D2CP00951J.